The Cryosphere

New radar altimetry datasets of Greenland and Antarctic surface elevation, 1991–2012

Maya Raghunath Suryawanshi[1,2]**, Malcolm McMillan**[1]**, Jennifer Maddalena**[1]**, Fanny Piras**[3]**, Jérémie Aublanc**[3]**,
Jean-Alexis Daguzé**[3]**, Clara Grau**[3]**, and Qi Huang**[1]

[1]UK Centre for Polar Observation & Modelling, Centre of Excellence in Environmental Data Science,
Lancaster Environment Centre, Lancaster University, Lancaster, LA1 4YW, UK
[2]Interdisciplinary Centre for Water Research, Indian Institute of Science, Bengaluru, India
[3]Collecte Localisation Satellites, 31520, Ramonville, France

Correspondence: Maya Raghunath Suryawanshi (maya2509.surya@gmail.com)

Abstract. Over the past three decades, there has been a 4.5-fold increase in the loss of ice from the Greenland and Antarctic Ice Sheets, resulting in an enhanced contribution to global sea level rise. Accurately tracking these changes in ice mass requires comprehensive, long-term measurements, which are only feasible from space. Satellite radar altimetry provides the longest near-continuous record of ice sheet surface elevation and volume change, dating back to the launch of ERS-1 in 1991, and maintained through the successive ERS-2, Envisat, CryoSat-2, and Sentinel-3 missions. To reliably constrain multi-decadal trends in ice sheet imbalance, and to place current observations within a longer-term context, requires continued efforts to optimise the processing of data acquired by the older historical missions and to evaluate the accuracy of these measurements. Here, we present new ERS-1, ERS-2, and Envisat altimeter datasets, comprising measurements of ice sheet elevation spanning two decades. This new observational record has been derived using consistent and improved retrieval methods, including enhancements to key Level-2 processing steps such as waveform retracking and echo relocation. Through comparison with independent airborne datasets, we undertake a comprehensive assessment of the accuracy of these measurements and demonstrate the improvements delivered relative to previously available products. With this updated processing, we find that all missions achieve sub-metre (<0.85 m) median elevation biases and dispersion of elevation differences relative to coincident airborne data. These new along-track datasets will be of benefit to a broad range of applications, including the quantification of ice sheet mass imbalance, investigations of the processes driving contemporary ice loss, and the constraint of numerical ice sheet models.

1 Introduction

Over the past three decades, the polar ice sheets have substantially increased their contribution to global sea level rise (The IMBIE Team, 2018, 2019), with the rate of ice loss expected to accelerate further as Earth's climate warms throughout the 21st century (Pörtner et al., 2019). Our understanding of both past changes and future projections of sea level rise benefit from long-term, multi-decadal observations of ice sheet evolution, in order to quantify historical changes in ice mass and to constrain and validate physical ice sheet models. Such continental-scale datasets are exclusively derived from satellite measurements, with polar-orbiting radar altimeters unique in their provision of near-continuous coverage of both polar ice sheets since the early 1990's. To date, these altimeters have provided a wealth of information relating to the geometry and evolution of the ice sheets, including ice sheet topography (Bamber et al., 2009, 2013; Helm et al., 2014; Slater et al., 2018; Otosaka et al., 2019), surface elevation changes (Helm et al. 2014; McMillan et al., 2014, 2016; Sørensen et al., 2018; Schröder et al., 2019; Shepherd at al., 2019), surface (Slater et al., 2021) and basal (Wingham et al, 2006; McMillan et al., 2013) processes, the location and migration of grounding lines (Dawson and Bamber, 2017; Hogg

et al., 2018; Konrad et al., 2018), and ice mass imbalance (Zwally et al., 2015; The IMBIE Team, 2018, 2019; Simonsen et al., 2021). These observations have played a key role in constraining and validating numerical model predictions, as auxiliary data in satellite processing chains, and for quantifying and understanding the drivers of ongoing sea level rise.

Radar altimeters were originally developed for ocean applications and, over time, their importance for ice sheet studies has been realised (de Q. Robin, 1966; Wingham et al., 1998, 2006a, b). The earliest high-inclination orbit missions of ERS-1, ERS-2, and Envisat all operated in a low-resolution mode (LRM), providing a relatively coarse (kilometre-scale) ground footprint and no information relating to the origin of the echo within the $\sim 16\,\mathrm{km}$ diameter beam limited footprint. Additionally, onboard tracking was not optimised for the rugged and highly complex surface topography found around the ice sheets' margins. As a result, ice sheet elevation measurements from these historical missions have typically been less accurate than those derived from more recent, higher-resolution radar altimeters such as CryoSat-2 and Sentinel-3 and the uncertainties associated with these measurements have been less well constrained. This, in turn, has made it more difficult to quantify the longer-term ice mass imbalance of Greenland and Antarctica, with certainty, and to place current observations within the context of the multi-decadal climate record.

In order to improve the fidelity and useability of measurements arising from these historical missions, episodic reprocessing of the altimeter archive is performed. This is designed to allow recent innovations in algorithms and auxiliary datasets to be utilised, even for missions which no longer actively acquire data. Until now, the most recent reprocessing of ERS-1, ERS-2, and Envisat data by the European Space Agency delivered the REprocessing Altimeter Products for ERS-1 and ERS-2 (REAPER) (Brockley et al., 2017), and the Envisat version 3 (Soussi et al., 2018) products. For ERS-1 and -2, REAPER integrated a number of improvements into the Level-1 and Level-2 processing chains, most notably the inclusion of the retrackers that had been implemented for Envisat processing, new precise orbit solutions, and refinements to the instrument calibration (Brockley et al., 2017). For Envisat version 3, improvements were made to a number of the geophysical corrections within the Level-2 processing, the definition of the continental ice flag, and the instrument calibration (Casella, 2018). Although these reprocessing activities represented significant advances in product quality at the time of their release, they are now more than 5 years old. As such, there is the potential to revisit and refine the algorithms implemented, in order to make use of more recent advances in methodology and computational resources. Within this study, which was performed within the context of the Fundamental Data Records for Altimetry (FDR4ALT) project funded by the European Space Agency, we therefore aim to (1) reprocess the ERS-1, ERS-2, and Envisat archives over both ice sheets in order to produce improved Level-2 and Level-2+ ice sheet elevation datasets spanning the period 1991–2012 and which consist of ice sheet elevation measurements sampled along the satellite track; (2) perform the most comprehensive assessment of measurement accuracy to date, across all three missions, using an extensive reference dataset; and (3) develop a new, dedicated Level-2+ Ice Sheet Thematic Data Product, which is designed to improve the future useability of this valuable historical record.

2 Data and methodology

In this section, we firstly introduce the principal characteristics of each of the satellite radar altimeters utilised in this study, together with the airborne data used for validation purposes. We then describe the methodology used to process the altimetry data, including both the principal Level-2 and thematic data product (TDP) algorithms. Finally, we summarise the approach employed to evaluate the accuracy of these new altimetry datasets.

2.1 ERS-1

The ERS-1 satellite was launched in 1991 with an orbital inclination of 98.6° and was the first altimeter to provide comprehensive coverage of the Greenland and Antarctic ice sheets. Over its lifetime, the mission operated in a number of different phases with differing lengths of repeat cycle, namely: a repeat cycle of 3 d (3 August 1991–4 April 1992 and 23 December 1993–10 April 1994), 35 d (4 April 1992–23 December 1993 and 21 March 1995–10 March 2000) and 168 d (10 April 1994–21 March 1995), as detailed in Table 1. As part of its primary payload, the satellite carried a Ku-band (13.6 GHz) radar altimeter, named RA. Although the mission finally ended in 2000, the radar altimeter was switched off in June 1996.

The ERS-1 radar altimeter operated in two possible tracking modes, "Ocean Mode" and "Ice Mode", corresponding to the two range resolution modes of the instrument. Designed with the purpose of maximising data retrieval over ice sheet surfaces, the Ice Mode had a number of dedicated characteristics, most notably deploying an increase in the range window width by a factor of four. This increased range window dimension had the effect of reducing the range gate resolution to approximately 1.82 m, as opposed to 0.45 m for the Ocean Mode. Acquisitions over ice sheets were almost exclusively made in Ice Mode, except for a few cycles of data. For a more extensive description of the specificities of each mode, the reader is referred to Peacock (1998).

2.2 ERS-2

The ERS-2 satellite was launched in 1995 and served as a follow-on mission to ERS-1, carrying an identically designed Ku-band radar altimeter (RA) instrument on board. How-

Table 1. ERS-1 orbit phases.

Name	Start	End	Repeat cycle
Launch	17 July 1991	–	–
Commissioning Phase (Phase A)	25 July 1991	10 December 1991	3 d
Roll Tilt Mode validation	12 December 1991	13 December 1991	35 d
Ice Phase (Phase B)	28 December 1991	1 April 1992	3 d
Roll Tilt Mode Campaign (Phase R)	4 April 1992	14 April 1992	35 d
Multidisciplinary (Phase C)	14 April 1992	21 December 1993	35 d
Second Ice Phase (Phase D)	23 December 1993	10 April 1994	3 d
Geodetic Phase (Phase E)	10 April 1994	28 September 1994	168 d
Geodetic Phase (Phase F)	28 September 1994	21 March 1995	168 d
Phase G 2nd Multidisciplinary	21 March 1995	17 August 1995	35 d
Phase G Tandem	17 August 1995	2 June 1996	35 d
Phase G Back-Up	2 June 1996	10 March 2000	35 d
End of mission	10 March 2000	–	–

ever, unlike ERS-1, the satellite operated a continuous 35 d repeat cycle throughout the entirety of its lifetime. Although the mission de-orbited in 2011, here we only process data up to June 2003 because the tape recorder failure at that time limited the subsequent geographical coverage to specific regions in close proximity to ground receiver stations (Milligan et al., 2008). Although several National Foreign Stations (NFS) were added between 2003 and 2011, coverage still remained limited and so we do not attempt to recover data after the tape recorder failure.

2.3 Envisat

Envisat was launched in 2002 and carried a dual frequency radar altimeter (RA2) which operated in C-band alongside the traditional Ku-band frequency. Like ERS-2, the mission maintained a 35 d repeat cycle throughout the entirety of its lifetime, which ended in April 2012. One of the most notable advances introduced by RA-2 was the model free tracker (MFT), which was designed to automatically adapt its resolution to the surface type. Envisat thus acquired data in three different acquisition modes; with high (320 MHz), medium (80 MHz), and low (20 MHz) bandwidths (Roca et al., 2009). Figure 1 illustrates the coverage of these modes for a single Envisat cycle, showing that over most of the ice sheet, Envisat provided a much higher range resolution (~ 0.47 m) than ERS-1 and ERS-2, which both acquired data predominantly in their Ice Mode (with a resolution of ~ 1.8 m). The exception to this was over the very margins of Antarctica and Greenland, where Envisat provided a similar (~ 1.9 m) or, at times, worse (~ 7.5 m) range gate resolution. A further distinction between Envisat and ERS-1/2 was the higher pulse repetition frequency (PRF) of the former. The 1795 Hz PRF of Envisat, which compared to 1020 Hz for ERS, resulted in a Level-1b waveform that was derived by averaging 100 individual pulses, allowing a greater reduction in radar speckle compared to the 50 pulse onboard averaging performed by

ERS-1/2. Finally, Envisat RA-2 waveforms were composed of 128 samples, in comparison to only 64 samples for ERS. This substantially increased the number of range gates that contained useful information, especially within the trailing edge of the echo.

2.4 Airborne data

The reference datasets that we use to validate the new ice sheet elevation products are airborne surface elevation measurements acquired by the Airborne Topographic Mapper (ATM) instrument, flown on-board NASA's Operation IceBridge (https://nsidc.org/data/icebridge/data, last access: 22 July 2025) and pre-IceBridge (https://nsidc.org/data/blatm2, last access: 22 July 2025) campaigns. Although airborne campaigns were less frequent over the ERS-1, ERS-2, and Envisat period than during the past decade, these datasets are the most extensive available and provide a valuable – and largely under-utilised – resource for assessing the accuracy of historical satellite products. For each mission, we therefore identify a cycle that coincides with an extensive airborne campaign over Greenland (Fig. 2) and use this as the basis for our validation activities. We selected Greenland for this validation exercise because it (1) offers far more extensive airborne data coverage than Antarctica, especially for pre-IceBridge campaigns, and (2) provides a broad range of topographic complexity and surface backscattering characteristics, over which it is beneficial to evaluate altimeter performance. Furthermore, we chose to focus on a single cycle, and did not look at changes in validation statistics through time, because the highly heterogeneous nature of sampling provided by airborne campaigns in different years would have limited such an intercomparison. In the following paragraphs we describe each of the datasets that were used in turn.

The Operation IceBridge Airborne Topographic Mapper (ATM) is an airborne scanning lidar developed by NASA to map ice surface elevation in the polar regions. Between
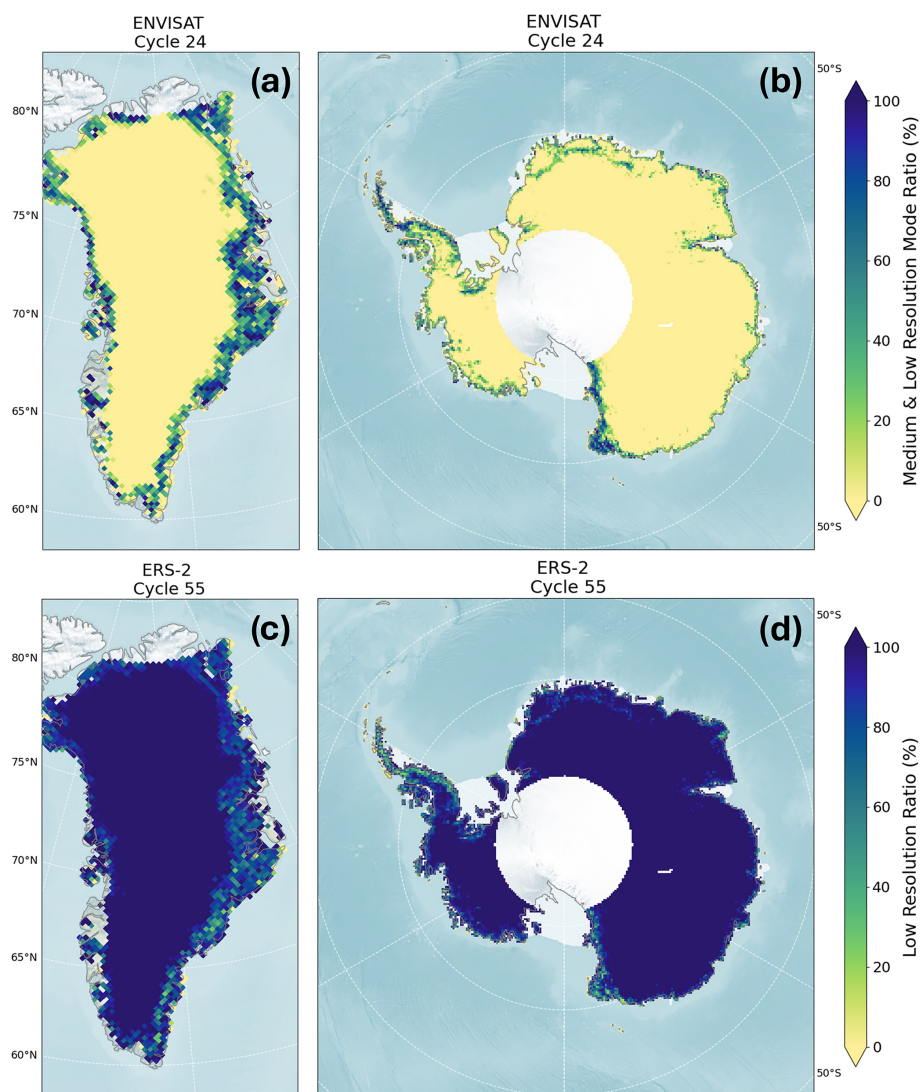
Figure 1. Panels **(a)** and **(b)** 1° × 1° gridded maps showing the distribution of Envisat low- and medium-range-resolution mode acquisitions (shaded blue) over Greenland **(a)** and Antarctica **(b)**, defined as the percentage of data where the measured bandwidth was either 80 MHz or 20 MHz. Panels **(c)** and **(d)** 1° × 1° gridded maps showing the distribution of the low-range-resolution mode acquisitions (shaded blue) for ERS-2, defined as the percentage of data where the measured bandwidth was 85 MHz.

2009 and 2020, it was one of the principal instruments carried onboard NASA's Operation IceBridge campaigns. The Level-2 elevation measurements have been resampled to approximately 50 m along-track (varying with aircraft speed) and have a fixed 80 m across-track platelet at aircraft nadir. At a nominal operating altitude (typically 500–750 m above the ice surface) the ATM elevation measurements have been estimated to achieve a horizontal accuracy of 74 cm, a horizontal precision of 14 cm, a vertical accuracy of 7 cm, and a vertical precision of 3 cm (Martin et al., 2012). Although the majority of Operation IceBridge campaigns have been flown since 2010, an extensive campaign was flown in the spring of 2009 (Fig. 2) and this dataset is of particular use for validating Envisat elevation measurements.

Prior to the initiation of Operation IceBridge in 2009, NASA's Wallops Flight Facility had flown Greenland airborne campaigns carrying ATM instruments in nearly every year since 1993. These ATM surface elevation measurements have a similar resolution to the ATM flown onboard Operation IceBridge, although typically offered a lower vertical accuracy of 20 cm (Krabill et al., 1995). We use these measurements to validate our ERS-1 and ERS-2 measurements of surface elevation over Greenland (Fig. 2).
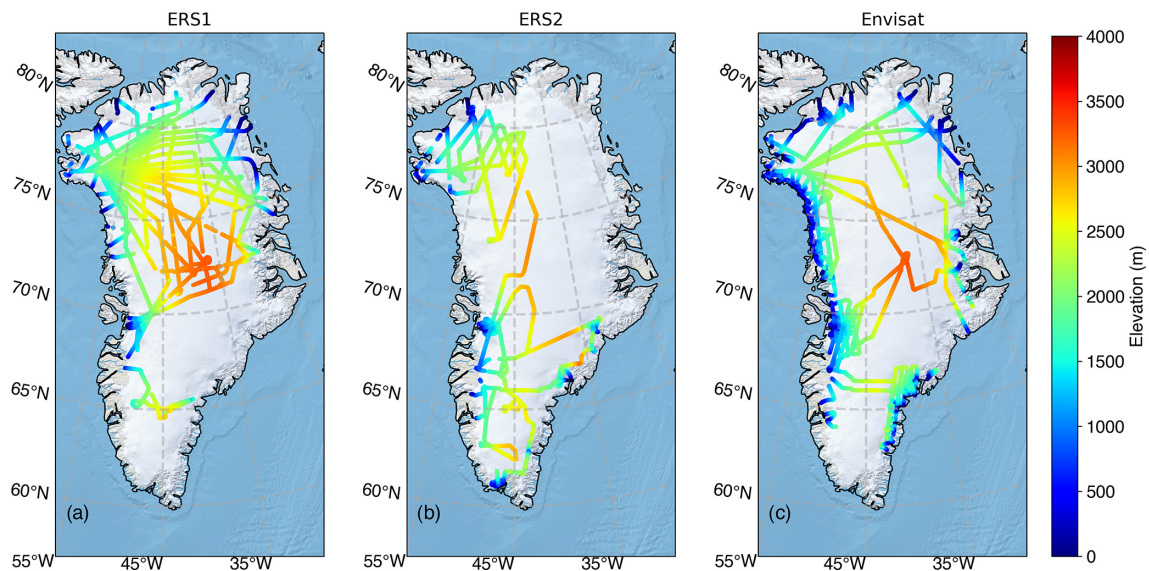
Figure 2. The airborne reference datasets acquired over Greenland that were used to validate the new altimetry products, for **(a)** ERS-1 (airborne campaign during May–June 1994), **(b)** ERS-2 (airborne campaign during May 2003), and **(c)** Envisat (airborne campaign during March–May 2009).

2.5 Altimetry processing methodology

2.5.1 Level-2 processing

The primary input data for this study were the ERS REAPER and Envisat V3.0 20 Hz waveforms. This section summarises the Level-2 processing and corrections that were then applied to estimate ice sheet elevation from these input products. A complete description of the algorithms is provided in the FDR4ALT Product User Guide (Piras et al., 2023) and the FDR4ALT Detailed Processing Model Document (The FDR4ALT team, 2023).

First, all ERS and Envisat measurements were selected over ice sheet surfaces, using the ice sheet masks from the BedMachine dataset (Antarctica v1.38 and Greenland v3.10; Morlighem et al., 2020). For each record, the ice sheet elevation was calculated as follows:

$$\text{elevation} = \text{altitude} - \text{altimeter\_range} - \sum \text{corr\_geophy}$$
$$+ \text{reloc\_correction}, \quad (1)$$

where altitude is the satellite altitude from the DEOS solution (Otten and Visser, 2019) and from the CNES release "F" of Precise Orbit Ephemerides (POE) standard (Picot et al., 2018), for ERS and Envisat respectively. The altimeter_range was derived from the window delay, adjusting for the position of the waveform within the acquisition window via the standard procedure of waveform retracking, using two different empirical retrackers that were evaluated within the study. The first retracker was an implementation of the threshold first maximum retracking algorithm (TFMRA) (Helm et al., 2014), with a retracking threshold of 25 %. The second was

the nominal retracking solution from the REAPER and Envisat V3.0 processors, which utilises an OCOG (ICE-1) retracker (Wingham et al., 1986; Bamber, 1994), with a retracking threshold of 30 % (Brockley et al., 2017). This retracker is referred to hereafter as the "threshold centre of gravity" (TCOG) retracker, in recognition of the fact that it is also employs a threshold-based approach. An intercomparison of these two retracking algorithms is reported in Sect. 2.6. The altimeter_range was also corrected for all instrumental corrections and accounts for the different gate resolutions induced by the acquisition modes that were described in Sect. 2.1 and 2.3.

To migrate measurements to their estimated origin on the ice surface, we adopted the methodology introduced by Roemer et al. (2007). This approach applies a correction in geographic position and height to relocate measurements to the point of closest approach (POCA), which is estimated from an auxiliary digital elevation model (DEM). Adopting this approach represents a significant algorithmic evolution compared to the slope based methods employed within the REAPER and Envisat version 3 processing configurations. More specifically, the Roemer methodology determines the POCA location by searching for the minimum satellite-surface range using a priori knowledge of the surface topography within the beam footprint, which is derived from the auxiliary DEM. The corresponding correction calculated during the relocation processing, reloc_correction, follows the formulation specified in Roemer et al. (2007). The auxiliary DEM's employed for the relocation processing were the Reference Elevation Model of Antarctica (REMA) v1.0 (Howat et al., 2019) and ArcticDEM v3.0 (Porter et al.,

2018) from the Polar Geospatial Center for measurements acquired over Antarctica and Greenland, respectively. Measurements where the estimated relocation distance exceeded 20 km from nadir were discarded and a warning flag was raised in cases where the relocation distance was between 8 and 20 km (8 km being the approximate boundary of the -3 dB antenna beamwidth). Figure 2 shows the relocation distances for a single cycle across Greenland and Antarctica.

In addition to the instrument and relocation corrections, a range of standard geophysical corrections were applied. Specifically, $\sum$ corr_geophy denotes the sum of all geophysical corrections applied and accounts for ionospheric and tropospheric delays and variations in range due to the pole tide, solid Earth tide, and ocean loading tide, together with corrections for ocean tide and the inverse barometer effect over floating ice. Full details relating to the models used are provided in the FDR4ALT Product User Guide (Piras et al., 2023).

Finally, two anomalies in the global ERS REAPER dataset were identified and corrected. First, the ERS REAPER dataset contains sporadic anomalies in the time tag field, which manifest as either a reversal in the normally monotonically increasing nature of consecutive measurements or a jump forward or backward in time. A dedicated algorithm was therefore developed to resolve these anomalies (detailed within the FDR4ALT Detailed Processing Model; The FDR4ALT team, 2023), which affected on average $\sim 1\%$ of the total dataset (Piras et al., 2023). Second, the presence of negative values in the REAPER waveform arrays was occasionally found to occur when the backscattered echo power reached high values, typically when the reflection originated from a specular surface. These values were corrected (The FDR4ALT team, 2023), which allowed an additional 0.3 %– 1.2 % of waveforms to be recovered depending on the mission and the time of the year.

2.5.2 Thematic data processing methodology

Following the Level-2 processing, an additional processing chain was implemented to derive an ice sheet thematic data product (TDP). This represented a new, higher-level, along-track addition to conventional Level-2 products. More specifically, this TDP chain takes ERS-1, ERS-2, and Envisat Level-2 elevation measurements as input and generates a more consistent elevation product at fixed nodes along reference ground tracks. The core methodology is based upon a repeat-track processing approach (e.g., Sørensen et al., 2011; Moholdt et al., 2010), whereby data are firstly partitioned into along-track segments and then corrected for the effect of topographic variability within each segment, which arises due to the orbital drift of the satellite. These additional steps are designed to deliver a more consistent along-track dataset that maintains the native 20 Hz sampling rate of the altimeter. Additionally, we also incorporate uncertainty estimation into the TDP chain, so that each resulting elevation measure-

ment has with it an associated uncertainty. In the following text, we summarise the main steps of the TDP chain and refer the reader to the FDR4ALT Detailed Processing Model (FDR4ALT team, 2023) for full details of the algorithmic implementation.

For each cycle, all Level 2 measurements acquired over Greenland and Antarctica are ingested and waveform quality flags and echo relocation flags are applied to remove poor quality records. An additional filter is applied to remove elevations that differ by more than 100 m from a reference DEM, specifically ArcticDEM for Greenland (Porter et al., 2018) and REMA for Antarctica (Howat et al., 2019). Typically, this filter removes at most 2 % of the ingested data. Next, a reference ground track is defined for each satellite pass, based upon the cycle which has a start point that is closest to the median of all start points of that pass. This reference track is then sampled at ~ 380 m intervals to create the reference nodes that form the common basis of the TDP product. For each reference track, a rectangular search window around each node is calculated, which has an along-track dimension equivalent to the reference node spacing (~ 380 m) and an across-track dimension (20 km) that is chosen to cover the maximum Level-2 relocation distance plus a buffer to account for the across-track orbit drift. This ensures that the search window will encapsulate all POCA measurements, irrespective of how far they have been migrated in the Level-2 echo relocation step.

For each search window along the satellite track, data from all cycles that fall within that search window are identified and associated with the respective reference node. In areas of high topographic relief, more than one POCA measurement per cycle can be segmented in a single search window. In this instance, the POCA measurement that is closest in elevation to its reference node (as determined using the DEM) is selected. In cases where multiple POCA measurements lie in a single search window and these POCA locations (and hence elevations) are identical, we cannot select a single measurement based upon the aforementioned criteria and hence the median of the elevation measurements is calculated.

Next, all POCA points for all cycles are migrated onto their associated reference nodes. In essence, this step corrects for the topographic difference in elevation between each POCA measurement location and the reference node location. The topographic difference in elevation is computed using a relatively coarse resolution version of the ArcticDEM (500 m) and REMA (200 m) products, so as to broadly align with the resolution of the pulse limited altimeter footprint. More specifically, for each POCA elevation, $z(i, j)$ at a location i, j, the migrated elevation $z(i', j')$ at the associated reference node location i', j' is given by

$$z\left(i', j'\right) = z(i, j) + \Delta z_{\text{topo}}(i, j), \tag{2}$$

where

$$\Delta z_{\text{topo}}(i, j) = z_{\text{DEM}}\left(i', j'\right) - z_{\text{DEM}}(i, j), \tag{3}$$
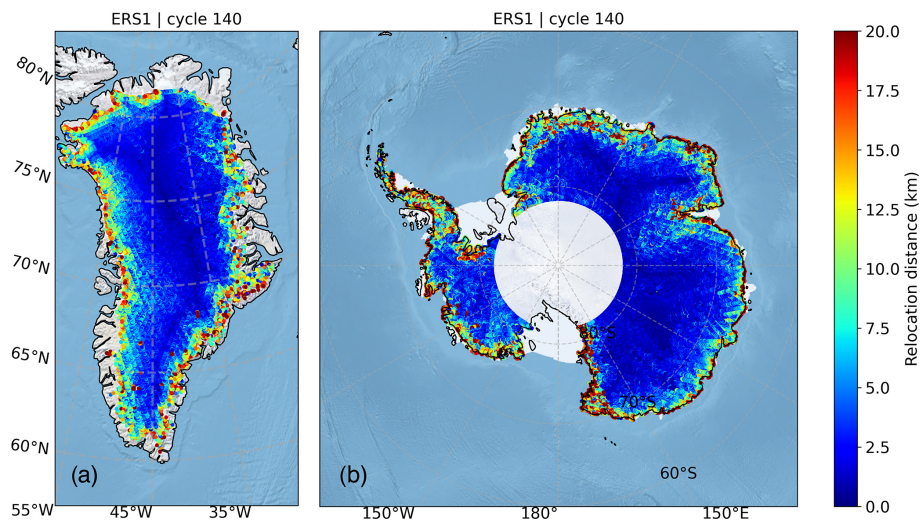
Figure 3. Spatial distribution of the relocation distance (the distance from satellite nadir to the point of closest approach) across the **(a)** Greenland and **(b)** Antarctic ice sheets for ERS-1 cycle 140.

and $z_{\text{DEM}}(i, j)$ and $z_{\text{DEM}}(i', j')$ are the DEM elevations at the POCA location and the reference node, respectively. Around the very margin of the ice sheet, in areas of extremely rugged topography, this topographic correction occasionally becomes unreliable. Therefore, if the magnitude of the topographic correction exceeds 200 m, then the correction is deemed unreliable and the corresponding elevation at the reference node is set to the fill value. Less than 1 % of the topographic corrections exceed 200 m ice-sheet-wide for both ice sheets and all cycles.

The uncertainty associated with each elevation measurement is estimated using an empirical parameterisation based upon elevation differences between near co-located (within 500 m) and near coincident (within 30 d) satellite and airborne measurements. Specifically, uncertainty is parameterised as a function of surface slope. This is motivated by the knowledge that measurement accuracy degrades as a function of ice sheet surface slope (McMillan et al., 2019) due to the challenges of retracking waveforms and identifying the correct echoing point over increasingly complex ice sheet terrain. More specifically, uncertainty is determined independently for each satellite mission by implementing the following processing steps. First, pairs of near co-located, near coincident airborne and satellite data are corrected for residual topographical differences due to any differences in location. Then satellite-minus-airborne elevation differences are computed for each pair. Next, an estimate of the magnitude of the surface slope at each comparison point is retrieved from an auxiliary DEM. An uncertainty look-up table is then defined by collating individual satellite-minus-airborne elevation differences within 0.1° slope bands and computing the median of the absolute elevation differences within each slope band. These median values typically lie in the range 0–10 m, depending upon the magnitude of the slope and the satellite

mission. At high slopes ($>1.3°$) the number of comparison points becomes small (<100 measurements per slope bin, on average; compared to 10^2–10^3 measurements per bin at lower slopes). As a result, the statistics for higher slope bins are relatively unstable, with a standard deviation typically 2–4 times higher. For slopes greater than 1.3°, we therefore assign uncertainties based upon a linear regression of uncertainty against slope with 0 intercept, which is fitted to the uncertainties computed at lower slopes ($<1.3°$). Finally, for each altimetry measurement, the surface slope is estimated at its echoing location and then the mission-specific look up table is used to assign an associated uncertainty to that altimetry measurement.

2.5.3 Neural network classification

It is well established (McMillan et al., 2021; Huang et al., 2024) that rugged ice sheet topography can introduce complexity into the shape of the returned waveform, which in turn can complicate the retrieval of estimates of ice sheet elevation. As such, analysing the morphologies of waveforms acquired over ice sheets can inform our understanding of the reliability of retrievals from different waveform classes. To this end, an existing supervised neural network classifier (Poisson at al., 2018) was first used to discriminate different Envisat Ku-band waveform shapes. Specifically, this algorithm has been designed to predict the most likely class for each echo based upon a subset of possible classes which are taken from a global reference dataset spanning all surface types and missions (Tables 2 and 3). Following Poisson et al. (2018), we selected 11 classes (1 to 9, 12, and 16) for the purposes of classifying and differentiating different types of Envisat waveform.

Table 2. Schematic drawings of the main waveform classes within the global reference dataset; descriptions of each class are provided in Table 3.
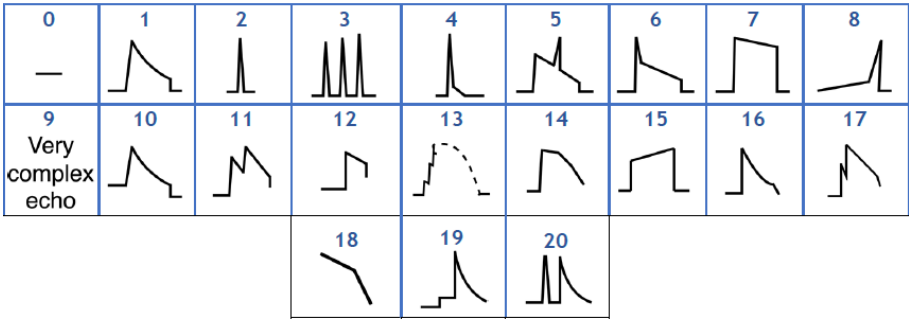

Table 3. Brief descriptions of the main waveform classes within the global reference dataset.

1	Brownian
2	Highly specular
3	Multiple peaks
4	Moderately specular
5	Brownian with a peak on the trailing edge
6	Brownian with a peak on the leading edge or a steep trailing edge
7	Brownian with a flat trailing edge
8	Strong peak at the end of the analysis window
9	Very complex echo
10	Brownian with high thermal noise
11	Double leading edge
12	Shifted Brownian
13	Brownian with a disturbed leading edge
14	Volume-Brownian
15	Linear rise
16	Right-shifted Brownian waveform
17	Breakage on the leading edge of a Brownian waveform
18	Linear decrease
19	Small step before leading edge
20	Peaky echo before Brownian echo

Building upon the work of Poisson et al. (2018), we also extended the same methodology for use with ERS-1 and ERS-2, developing a new supervised neural network that was trained and validated using radar waveforms from these missions. This represents a significant advance compared to the previous REAPER products, which did not have any such waveform shape classification and instead included only a set of flags providing the user with waveform quality checks relating to whether the altimeter recorded significant power within the tracking window. In terms of our implemented classification approach, the initial learning step consisted of labelling thousands of waveforms (see Table 4) that were acquired over the broadest range of surface types (land ice, inland water, and open, coastal, and polar ocean) and in different operating modes, in order to capture the full variety of surface slope, roughness, and backscattering characteristics. This step utilised data from January 1996 for both ERS-1 and ERS-2 (respectively cycle 8 and cycle 153) and allowed us to

determine the subset of classes applicable to the RA altimeter, according to Table 2. Due to the differences in instrument design between RA and RA-2 (as detailed in Sect. 2.1), which impact upon the waveform range resolution and shape, the relevant classes are not identical, and we find that for RA the most relevant classes are 1–7, 9–11, 13 and 15–18.

The second step was to determine the set of geometrical parameters describing the RA waveform to be used as input to the neural network. Indeed, we did not consider the whole waveform as input but the following set of 11 waveform parameters: (1) leading edge slope, (2) trailing edge slope, (3) thermal noise slope, (4) amplitude of the main peak on the trailing edge and (5) the thermal noise, (6) a breakage flag on the leading edge, (7) the centre of gravity of the waveform, (8) the mean square difference between a mean ocean waveform and each measurement, and (9) the global peakiness, (10) kurtosis, and (11) skewness. To assess the performance of the neural network in predicting classes, the

collected dataset was split into two strictly independent subsets for training (10 616 waveforms) and testing (3982 waveforms) representing 73 % and 27 % of the manually collected dataset, respectively (Table 4). We considered ocean class 1 to be the most represented class (46 % of the dataset), as oceans cover most of Earth's surface, but not more than 50 % to avoid over-fitting.

The network itself was designed as a feed-forward single-layer neural network and was built using the R package *nnet* (Venables and Ripley, 2002), with 11 neurons in the input layer, 25 in the hidden layer, and 15 as outputs. We used a *softmax* activation function in the output layer to generate the probability that a given waveform belongs to the respective classes and a decay value of 1×10^{-12} to prevent from over-fitting. The performance of the neural network classifier was assessed using the test database and results are presented in Table 5 for the most dominant classes over ocean and ice regions. In line with the training strategy, the classifier was then run globally during the inference phase to ensure a globally-consistent solution irrespective of surface type. Full results relating to other surface types are available in the FDR4ALT Product Validation Report (Simeon et al., 2023) and further details of the algorithm are provided in the FDR4ALT Detailed Processing Model (FDR4ALT team, 2023) document.

2.6 Level-2 validation methodology

To evaluate the accuracy of the newly processed altimetry datasets, we computed elevation differences relative to co-located, contemporaneous airborne data. Specifically, for each satellite mission we evaluated Level-2 elevation measurements derived from three different altimeter processing configurations: the existing REAPER (Brockley et al., 2017) and Envisat version 3 (Soussi et al., 2018) products available from the European Space Agency together with output from the new FDR4ALT processing chain, which included two different retracking solutions. Further details are provided in Table 6. This intercomparison was designed to provide a systematic benchmarking of each of the new datasets against existing products to assess whether they offered an improvement in measurement accuracy.

To evaluate each processing configuration, we first identified all airborne measurements acquired within a 500 m search radius (i.e. less than half the altimeter's nominal pulse limited footprint) and within 30 d of each satellite measurement. We then used these to compute elevation differences (satellite-minus-airborne) between each pair. This method is similar to that reported in McMillan et al. (2019), except that here we also introduced a temporal constraint on the search to avoid the need to correct for temporal changes in elevation. To limit the inclusion of anomalous data, we removed airborne elevation measurements that were greater than 5000 m, applied retracking (ICE-1, TFMRA) quality flags and our Roemer relocation slope correction flag (limiting the relocation distances up to 20 km) to the altimeter

products, and removed outlying altimetry measurements that deviated by more than 100 m from a reference DEM. We then corrected for the effect of topographic variations within the 500 m search radius using an auxiliary DEM. Finally, we calculated estimates of the overall bias (median) and dispersion (MAD; median absolute deviation from the median) of elevation differences for each mission relative to the reference data and the proportion of outliers (defined as elevation differences with a magnitude exceeding 10 m). We also investigated the relationship between the magnitude of the elevation differences and geophysical parameters such as surface slope and altimeter waveform shape.

3 Results and discussion

In this section, we firstly assess the coverage offered by our new FDR4ALT datasets. Next, we evaluate the accuracy of the Level-2 elevation measurements with respect to airborne reference data and compare this to the accuracy of the pre-existing REAPER and Envisat version 3 products. We then assess waveform morphology over the ice sheets, using our neural network classification to investigate the impact of waveform morphological type upon the accuracy of the elevation retrievals. Finally, we analyse the characteristics of the thematic data product, which applies additional processing steps that are designed to improve the homogeneity of the data for the end user.

3.1 Spatial coverage

First, we evaluated the spatial coverage provided by each mission and the different processing scenarios. For this analysis, we selected one 35 d repeat cycle for each mission: cycle 155 (24 March to 28 April 1996) of ERS-1, cycle 77 (26 August to 30 September 2002) of ERS-2, and cycle 78 (6 April to 11 May 2009) of Envisat, to ensure a comparable orbital sampling pattern across all missions. An overview of the coverage is shown in Fig. 4. Although coverage is broadly comparable across all processing scenarios, close to the ice margin the new FDR4ALT solutions exhibit less continuous along-track sampling, due to the ability of the Roemer relocation approach to more precisely identify the point of closest approach in regions of rugged topography, and thus to preferentially track local topographic highs within the beam footprint. This is expected to be more realistic than slope-based methods in regions of complex topography, where the point of closest approach is sensitive to smaller wavelength topographic features within the altimeter beam footprint in addition to the large-scale slope.

Secondly, we assessed the sampling provided by each mission within different bands of ice sheet surface slope (Fig. 5) by computing the proportion of 2×2 km grid cells that contained at least one valid elevation measurement. Within the low-slope interior of the ice sheet, the 35 d orbit yields

Table 4. The number of labelled waveforms for each class for both training and testing datasets.

Class	1	2	3	4	5	6	7	9
Training	4723	363	240	1096	710	1648	252	279
Testing	2023	121	80	365	236	549	84	92

Class	10	11	13	15	16	17	18
Training	153	160	212	132	189	312	147
Testing	51	53	70	43	63	103	49
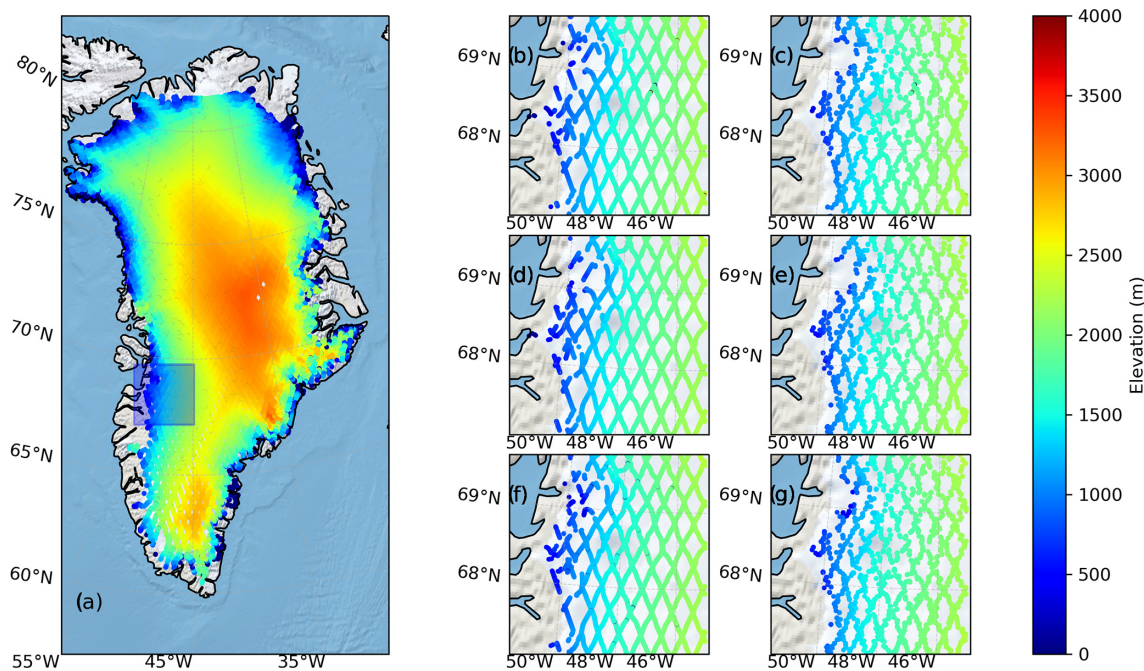
Figure 4. Comparison of the coverage of elevation measurements provided by different processing configurations and missions over the Greenland Ice Sheet (panel **a**) and the Russell Glacier region of Western Greenland (panels **b–g**). Panel **(a)** shows the coverage provided by the FDR4ALT processing with TCOG retracking for Envisat cycle 78. Panels **(c)** to **(g)** show the coverage provided over the Russell Glacier region in Western Greenland (blue box marked on **a**) by the ERS-1 REAPER **(b)** and FDR4ALT TCOG **(c)** cycle 155; ERS-2 REAPER **(d)** and FDR4ALT TCOG **(e)** cycle 77; and Envisat version 3 **(f)** and FDR4ALT TCOG **(g)** cycle 78 products.

Table 5. Performance of the neural network classifier on the test database for ocean Brownian waveforms (class 1), peaky waveforms (classes 2 and 4), and sharp Brown-like waveforms (class 6).

Class	1	2	4	6	others
Success (%)	95.4	87.6	88.0	88.4	60
Failure (%)	4.6	12.4	12.0	11.6	40
Total (%)	100	100	100	100	100

$\sim 7\,\%$–$8\,\%$ coverage of grid cells, which progressively decreases with higher slope. For more highly sloped regions (slopes in the range 1.5–2°; constituting $\sim 6\,\%$ of ice sheet grid cells), for example, coverage is typically below 2 % for all missions. It is important to note, however, that the percentages are dependent upon the size of grid used, and using a coarser resolution grid would result in higher percentage values. Here we choose 2×2 km to be approximately equivalent to the size of the pulse limited altimeter footprint. Comparing the relative coverage provided by the three missions we find that they are similar overall, albeit at higher slopes there is a small progressive improvement from ERS-1, to ERS-2, and to Envisat (Fig. 5).

3.2 Level-2 accuracy assessment

3.2.1 Envisat

We assessed the accuracy of both the existing Envisat version 3 product and the new FDR4ALT Level-2 datasets (the

Table 6. Satellite data and processing configurations used in the comparison with airborne data.

Processing configuration	Satellite	Relocation method	Retracker cycle	Validation	Validation date
E1 REAPER	ERS-1	Linear slope (Brockley et al., 2017)	ICE-1 (Brockley et al., 2017)	140	May 1994–September 1994
E1 ROEMER + TCOG	ERS-1	Roemer (Roemer et al., 2007)	TCOG (Brockley et al., 2017)	140	May 1994–September 1994
E1 ROEMER + TFMRA	ERS-1	Roemer (Roemer et al., 2007)	TFMRA (based on the algorithm definition of Helm et al., 2014)	140	May 1994–September 1994
E2 REAPER	ERS-2	Linear slope (Brockley et al., 2017)	ICE-1 (Brockley et al., 2017)	84	April 2003–June 2003
E2 ROEMER + TCOG	ERS-2	Roemer (Roemer et al., 2007)	TCOG (Brockley et al., 2017)	84	April 2003–June 2003
E2 ROEMER + TFMRA	ERS-2	Roemer (Roemer et al., 2007)	TFMRA (based on the algorithm definition of Helm et al., 2014)	84	April 2003–June 2003
EV GDR V3	Envisat	Linear slope (Soussi et al., 2018)	ICE-1 (Soussi et al., 2018)	78	April 2009–May 2009
EV ROEMER + TCOG	Envisat	Roemer (Roemer et al., 2007)	TCOG (Soussi et al., 2018)	78	April 2009–May 2009
EV ROEMER + TFMRA	Envisat	Roemer (Roemer et al., 2007)	TFMRA (based on the algorithm definition of Helm et al., 2014)	78	April 2009–May 2009
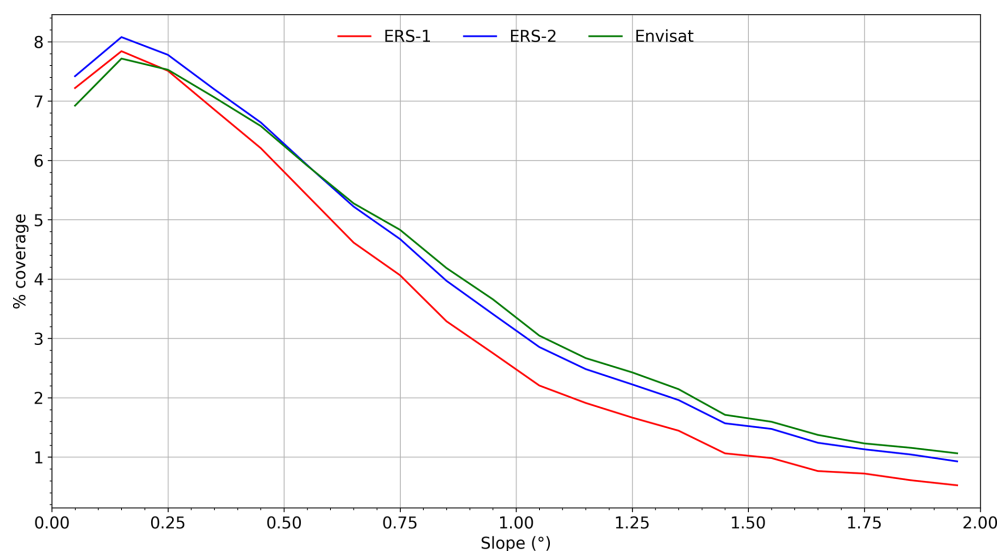
Figure 5. The coverage provided by each mission over the Greenland Ice Sheet as a function of ice sheet surface slope. The coloured lines represent the percentage of 2 km grid cells sampled by at least one valid measurement from ERS-1 cycle 155, ERS-2 cycle 77, and Envisat cycle 78.
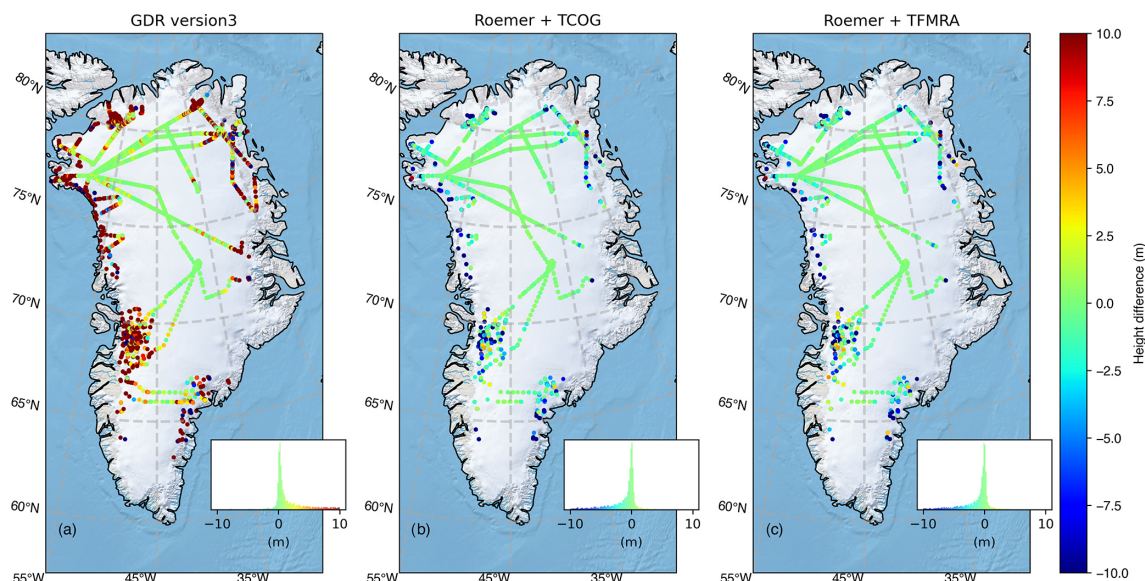
Figure 6. Comparison of elevation differences (Envisat minus airborne) over the Greenland Ice Sheet for the different processing configurations of Envisat cycle 78. Namely, the baseline version 3 product (panel **a**), the FDR4ALT Roemer + TCOG configuration (panel **b**), and the FDR4ALT Roemer + TFMRA configuration (panel **c**). The inset panels show the distribution of elevation differences for each processing configuration.
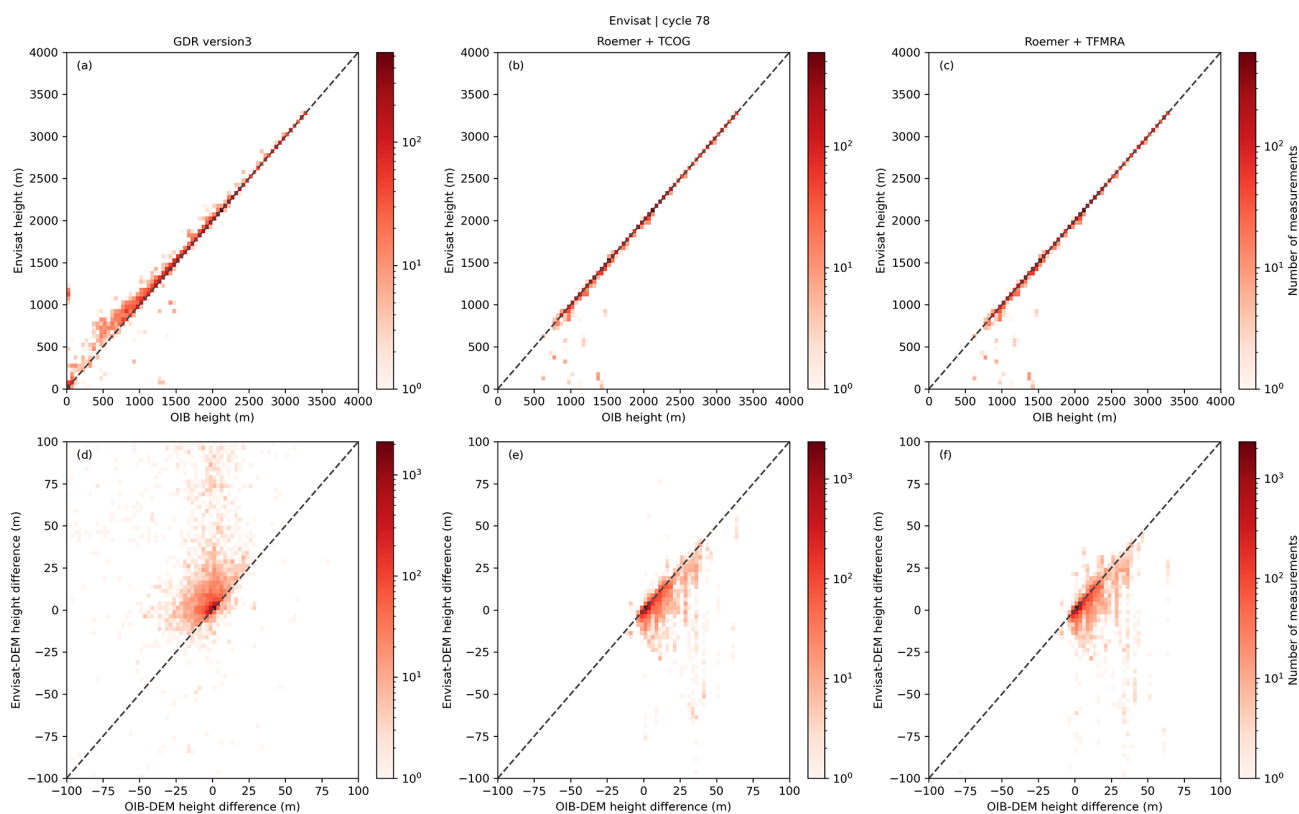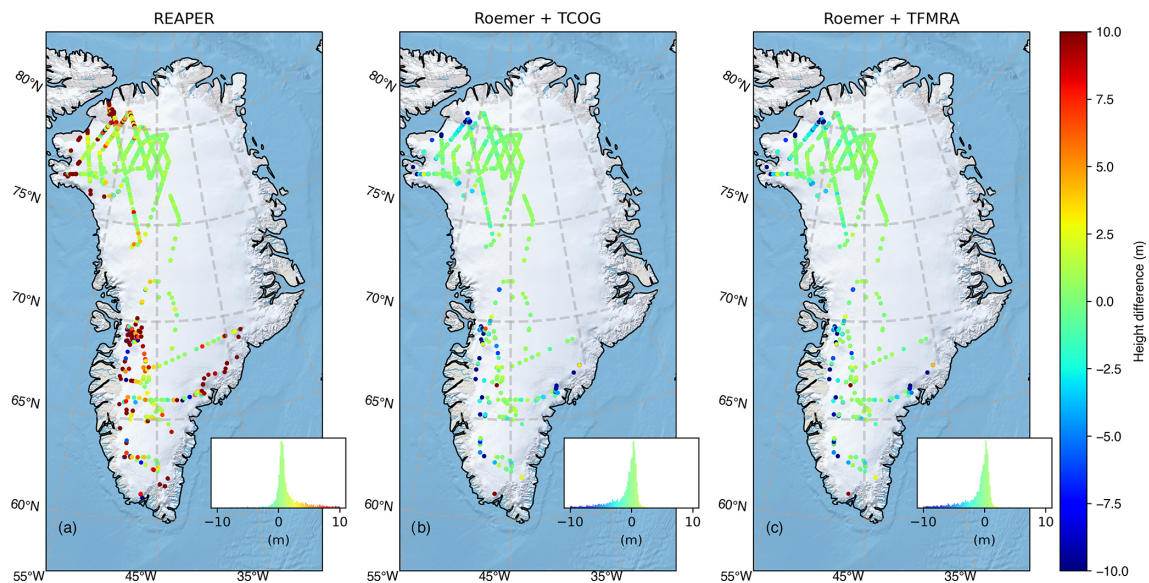

Figure 7. Density scatter plots showing the distributions of elevation measurements at locations sampled contemporaneously by both the Envisat and Operation IceBridge (OIB) airborne platforms. The top row (panels **a**–**c**) shows the original elevations; the bottom row (panels **d**–**f**) shows elevation residuals relative to an auxiliary DEM, which was used to remove the large-scale topographic variance.

Figure 8. Comparison of elevation differences (ERS-2 minus airborne) over the Greenland Ice Sheet, for the different processing configurations of ERS-2 cycle 84; namely, the REAPER product (panel **a**), the FDR4ALT Roemer + TCOG configuration (panel **b**), and the FDR4ALT Roemer + TFMRA configuration (panel **c**). The inset panels show the distribution of elevation differences for each processing configuration.
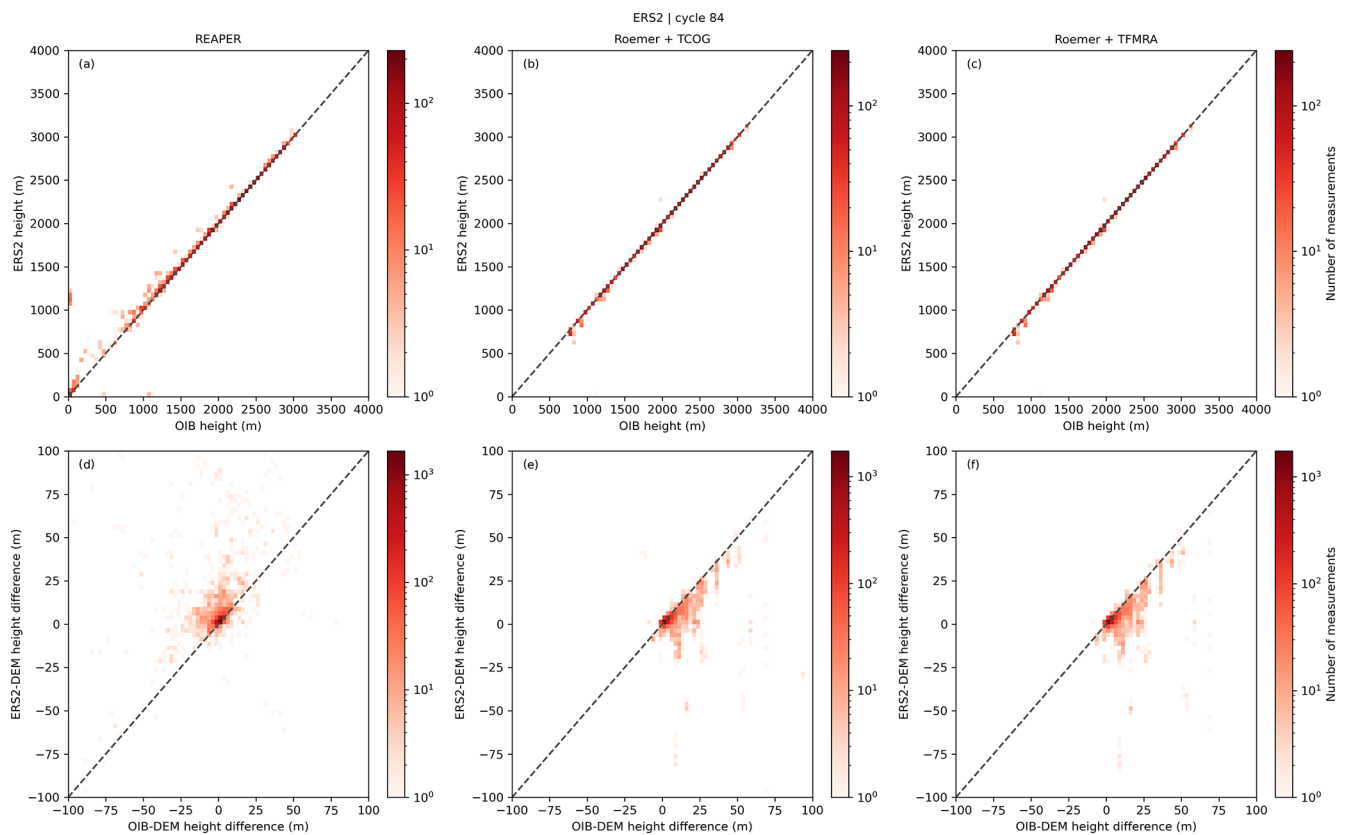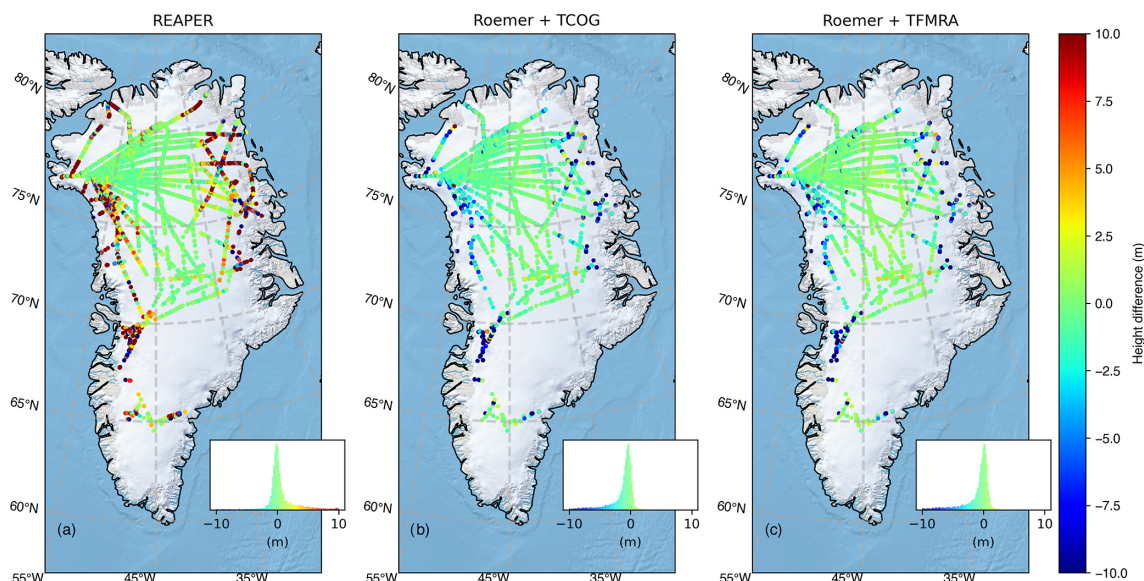

Figure 9. Density scatter plots showing the distributions of elevation measurements at locations sampled contemporaneously by both the ERS-2 and Operation IceBridge (OIB) airborne platforms. The top row (panels **a–c**) shows the original elevations; the bottom row (panels **d–f**) shows elevation residuals relative to an auxiliary DEM, which is used to remove the large-scale topographic variance.

Figure 10. Comparison of elevation differences (ERS-1 minus airborne) over the Greenland Ice Sheet, for the different processing configurations of ERS-1 cycle 140; namely, the REAPER product (panel **a**), the FDR4ALT Roemer + TCOG configuration (panel **b**), and the FDR4ALT Roemer + TFMRA configuration (panel **c**). The inset panels show the distribution of elevation differences for each processing configuration.
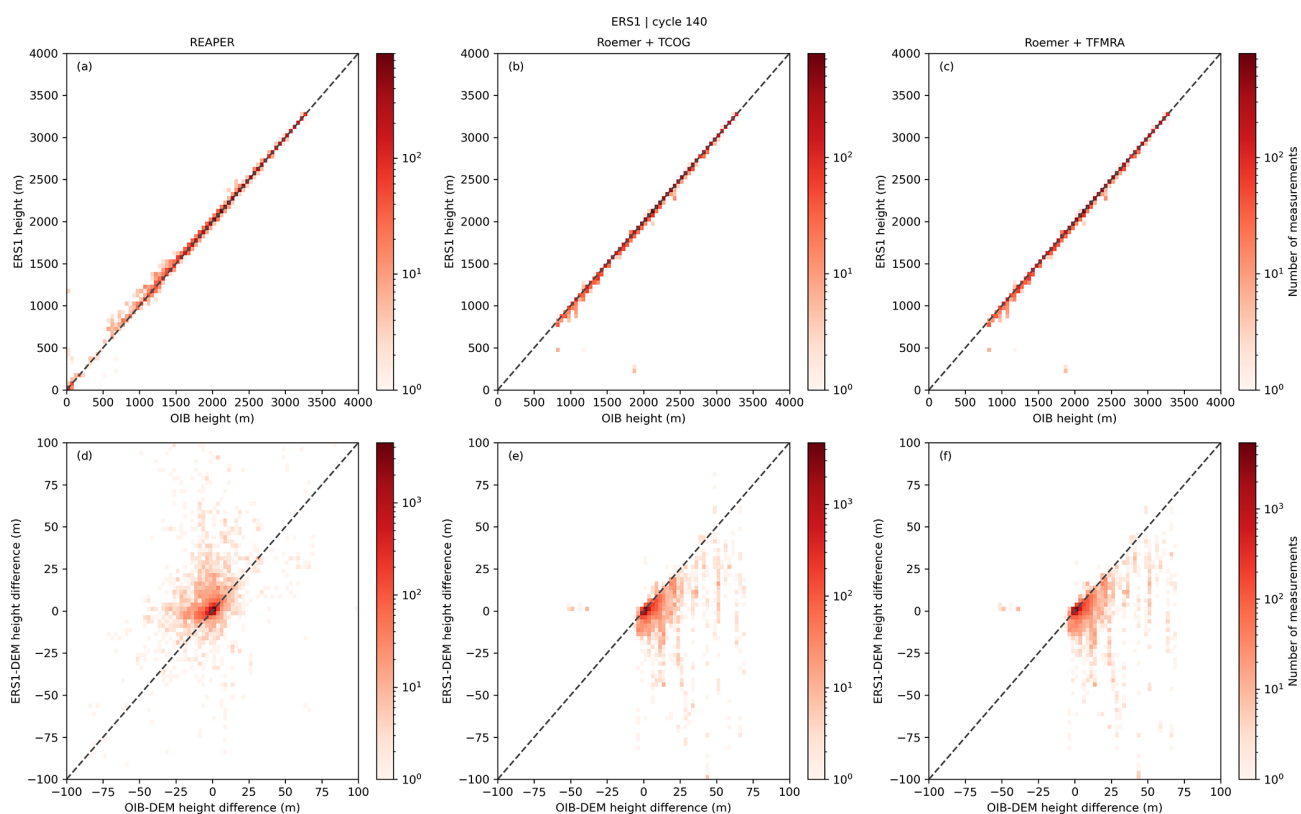

Figure 11. Density scatter plots showing the distributions of elevation measurements at locations sampled contemporaneously by both the ERS-1 and Operation IceBridge (OIB) airborne platforms. The top row (panels **a**–**c**) shows the original elevations; the bottom row (panels **d**–**f**) shows elevation residuals relative to an auxiliary DEM, which is used to remove the large-scale topographic variance.
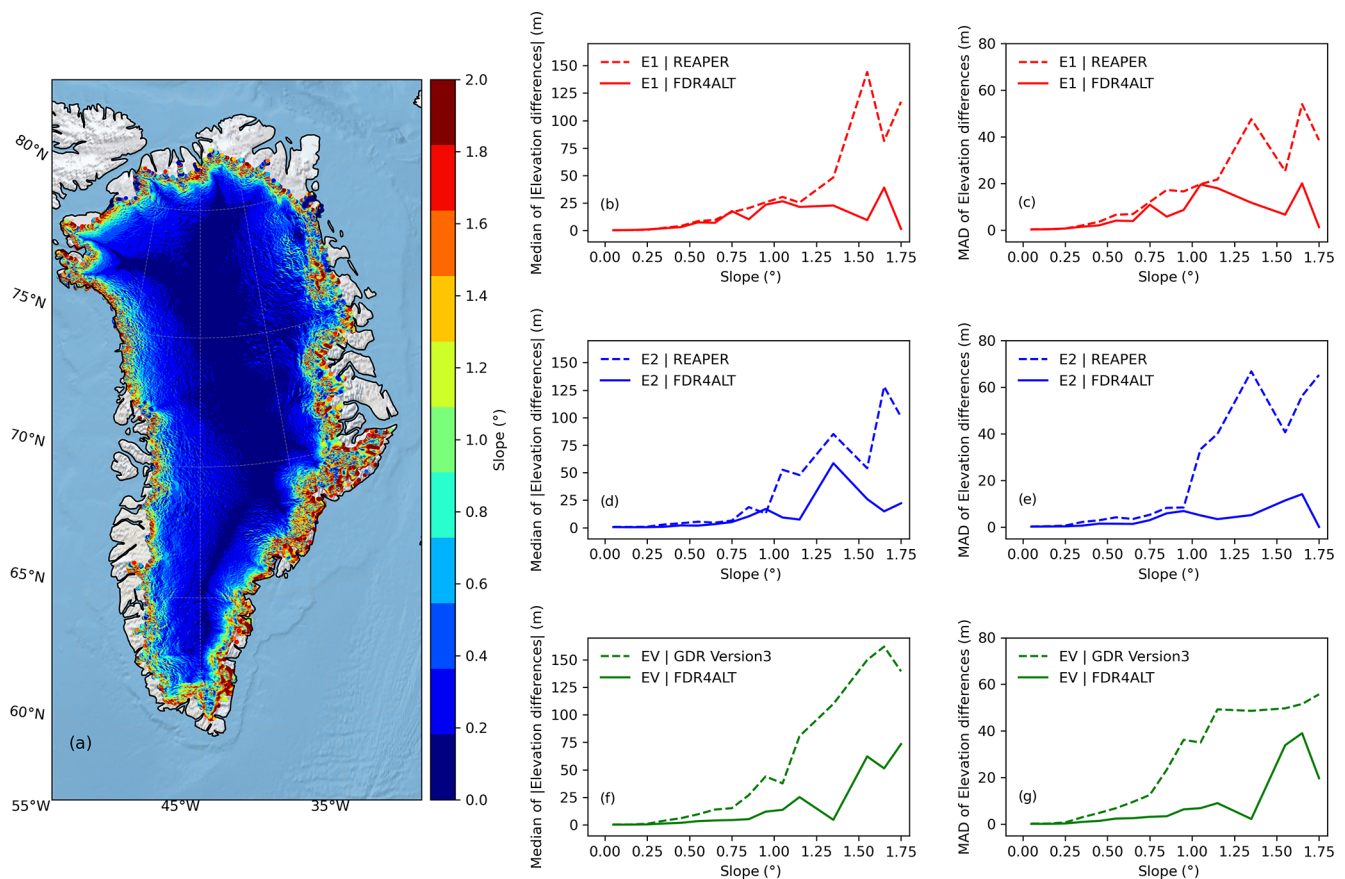
Figure 12. Comparison of baseline (REAPER and Envisat version 3) and FDR4ALT measurement accuracy as a function of Greenland Ice Sheet surface slope, through comparison to airborne reference datasets. A retracking quality flag was applied to all three products and, in the case of FDR4ALT, a relocation flag was also applied. **(a)** Surface slope of the Greenland Ice Sheet; **(b)** and **(c)** the median absolute elevation difference **(b)** and the median absolute deviation (MAD) from the median of the elevation differences **(c)** as a function of surface slope for ERS-1 REAPER (dashed line) and FDR4ALT TCOG (solid line) datasets. Panels **(d)** and **(e)** provide the same information as **(b)** and **(c)**, but for ERS-2. Panels **(f)** and **(g)** provide the same information as **(b)** and **(c)**, but for Envisat.

latter of which includes two retracking solutions; TCOG retracking and TFMRA retracking) through comparison with our airborne reference dataset. The spatial pattern of elevation differences is shown in Fig. 6, with the overall distributions of the differences provided in the inset panel. Whilst all solutions perform well within the lower slope interior of the ice sheet, it is clear that both of the FDR4ALT solutions exhibit a reduced number of large outliers in regions close to the ice margin. This contrasts with the existing version 3 product, which commonly exhibits elevations that deviate by more than 10 m from the coincident airborne data (Fig. 6a). This is reflected in the large (∼ 20 %) reduction in the percentage of FDR4ALT comparison points classified as outliers (∼ 14 %) as compared to the equivalent statistic for the version 3 product (∼ 35 %; Table 7). Even within the interior of the ice sheet, improvements are evident in the FDR4ALT solutions relative to GDR version 3, with a number of the inland tracks exhibiting fewer outliers. Overall, there are significant reductions in both the bias and the dispersion statistics for

the FDR4ALT products, with the FDR4ALT elevation bias reduced by 78 % relative to version 3 and the dispersion reduced by 67 % relative to version 3 (Table 7).

Figure 7 presents the same comparison data as density scatter plots and illustrates the level of agreement between the retrieved satellite elevations and the coincident airborne elevations (panels a–c). This assessment shows that, at low elevations, the existing version 3 product suffers from an increasingly positive bias (evident from the divergence away from the 1–1 line). In contrast, due to a combination of the more sophisticated echo relocation and more stringent quality control, neither of the two FDR4ALT configurations shows the same artefacts. Because the overall variance in ice sheet elevation due to its topography (∼ 0–3500 m) is much larger than the variance between the altimeter and airborne measurements, we also use an auxiliary digital elevation model to remove the large-scale topographic variation that is common to both datasets. This isolates more clearly the residual differences between the airborne and altimeter
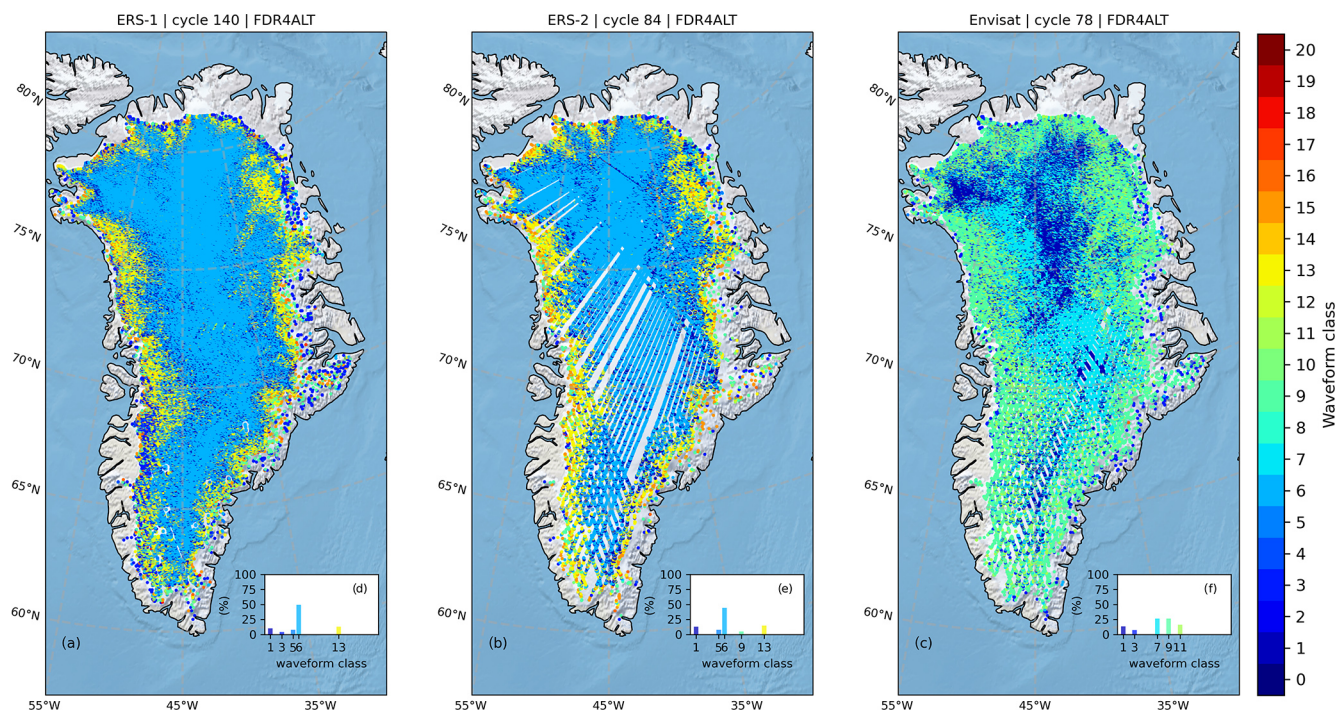
Figure 13. The spatial distribution of waveform classes over the Greenland Ice Sheet for one orbital cycle of ERS-1 **(a)**, ERS-2 **(b)**, and Envisat **(c)**. In each of the main panels, data have been aggregated onto a 2×2 km grid, with the modal value of all data within a given cell shown. The inset figures show the percentage of grid cells covered by each of the top five waveform classes for each mission. The different waveform classes are defined in Table 8.
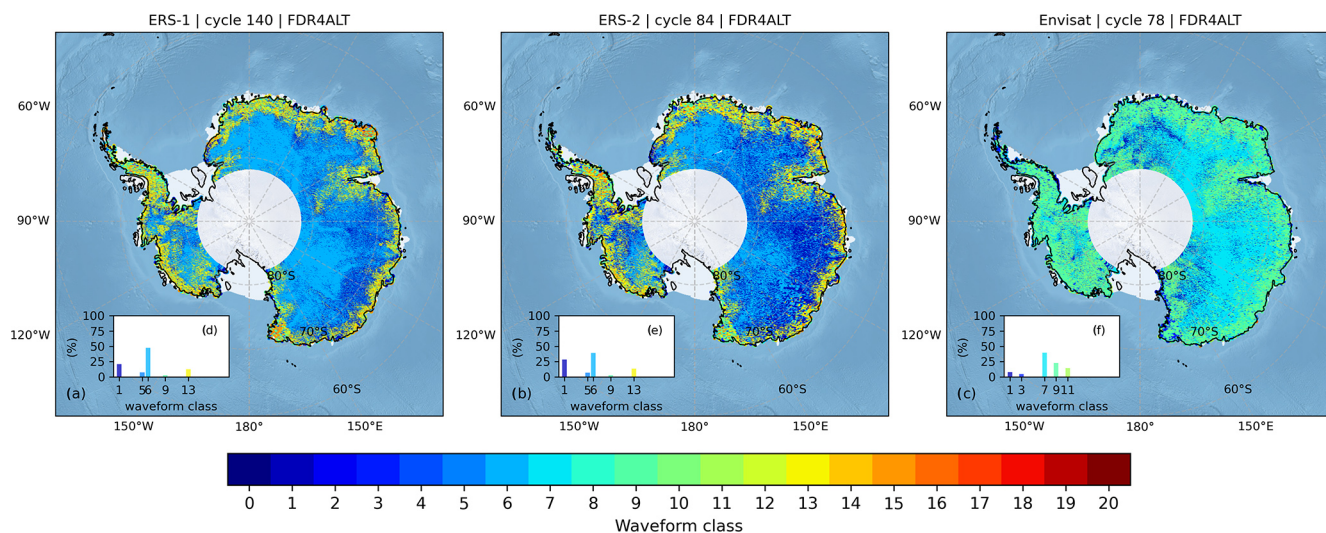

Figure 14. The spatial distribution of waveform classes over the Antarctic Ice Sheet for one orbital cycle of ERS-1 **(a)**, ERS-2 **(b)**, Envisat **(c)**. In each of the main panels, data have been aggregated onto a 2×2 km grid, with the modal value of all data within a given cell shown. The inset figures show the percentage of grid cells covered by each of the top five waveform classes for each mission. The different waveform classes are defined in Table 9.
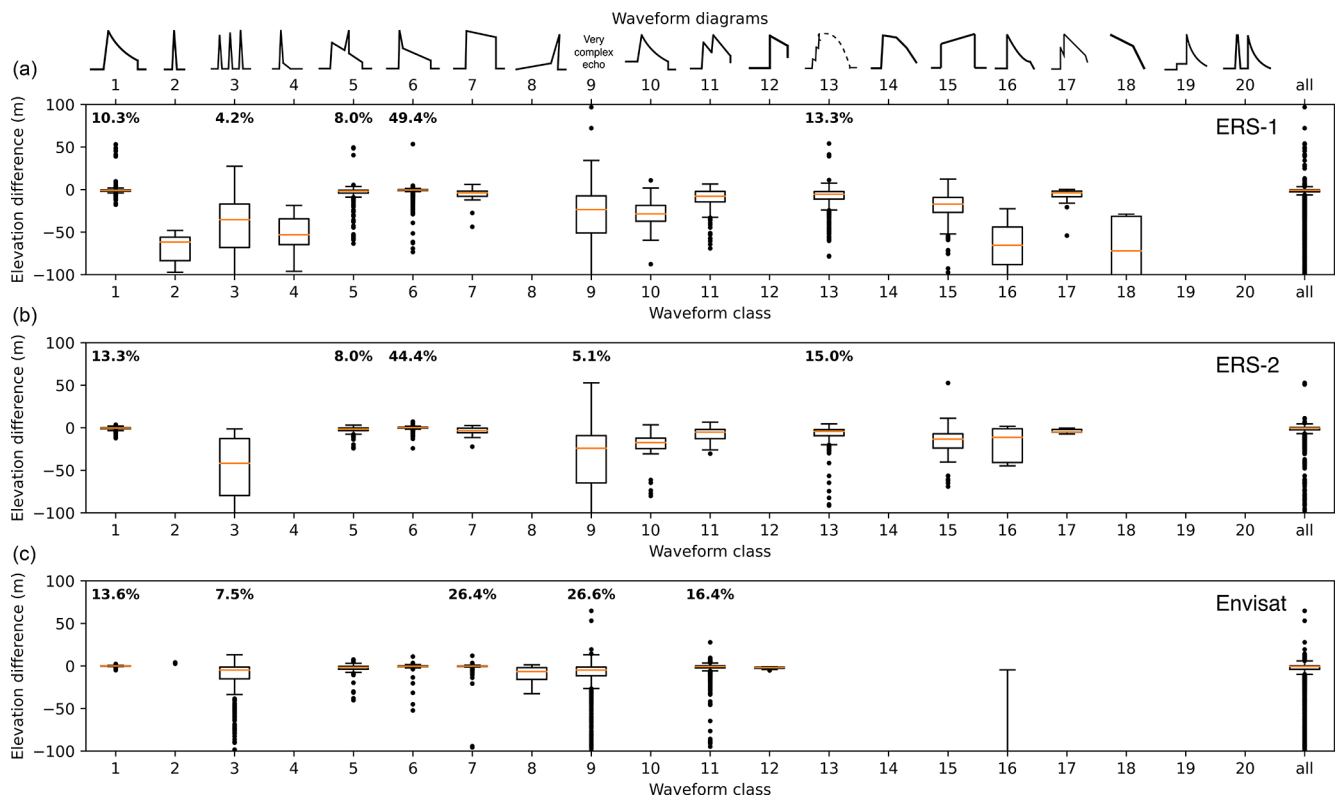
Figure 15. Box and whisker plots representing the distributions of elevation difference (mission minus airborne) for each of the waveform classes obtained from the neural network classification, for ERS-1 **(a)**, ERS-2 **(b)**, and Envisat **(c)**. On each plot, the orange line denotes the median elevation difference, the boxes represent the lower and upper quartiles, the whiskers indicate the range spanned by 99 % of the data, and the circles locate the remaining outliers. As described in the methods, classes 8, 12, 14, 19 and 20, and classes 10, 13–15, and 17–20 are excluded for the ERS and Envisat missions, respectively. The percentage of waveforms within the five most common classes are given in bold for each mission.

measurements (Fig. 7d–f). This shows that there are a greater number of positive elevation artefacts present in the version 3 dataset (Fig. 7d) that are absent from the FDR4ALT solutions (i.e. the power rising vertically upwards from the origin in panel d). Finally, comparing the two FDR4ALT configurations (TCOG and TFMRA) indicates that similar results are achieved for both retrackers. Overall, there is less than 0.02 m difference in both the bias and the dispersion, although TCOG does slightly reduce the number of large outliers, with a 1.3 % reduction in the number of comparison points deviating by more than 10 m from the airborne measurement (Table 7).

3.2.2 ERS-2

Next, we performed the same comparative analysis for ERS-2. Figure 8 shows maps of ERS-2 elevation differences with respect to the reference data, and Fig. 9 presents density scatter plots of their respective distributions. As was the case for Envisat, whilst all solutions again perform relatively well within the lower slope interior of the ice sheet, both FDR4ALT datasets exhibit a reduced number of out-

liers close to the margin. This is evident as a 7 % reduction in the percentage of FDR4ALT comparison points that have an absolute elevation difference greater than 10 m (9.5 % for the FDR4ALT product, compared to 16.8 % for the REAPER product; Table 7). In terms of the central part of the distribution, we again find that the FDR4ALT solutions outperform REAPER, most notably providing a 73 % reduction in the magnitude of the bias (from +0.93 to −0.25 m, in the case of the FDR4ALT TCOG solution). Additionally, the FDR4ALT solution also yields a modest (3.4 %) improvement in the MAD dispersion (Table 7).

Figure 9 shows the same comparison data, displayed as density scatter plots that compare the retrieved satellite elevations and the coincident airborne elevations (panels a–c). This shows a similar pattern to Envisat, with REAPER exhibiting an increasingly positive bias at lower elevations, albeit the divergence is not as pronounced as was the case for Envisat (Fig. 7). Mirroring the results for Envisat, the FDR4ALT solutions successfully remove this artefact. Comparing the two FDR4ALT configurations themselves again shows relatively small differences between the two retracking solutions (Table 7), albeit with the TCOG solution show-
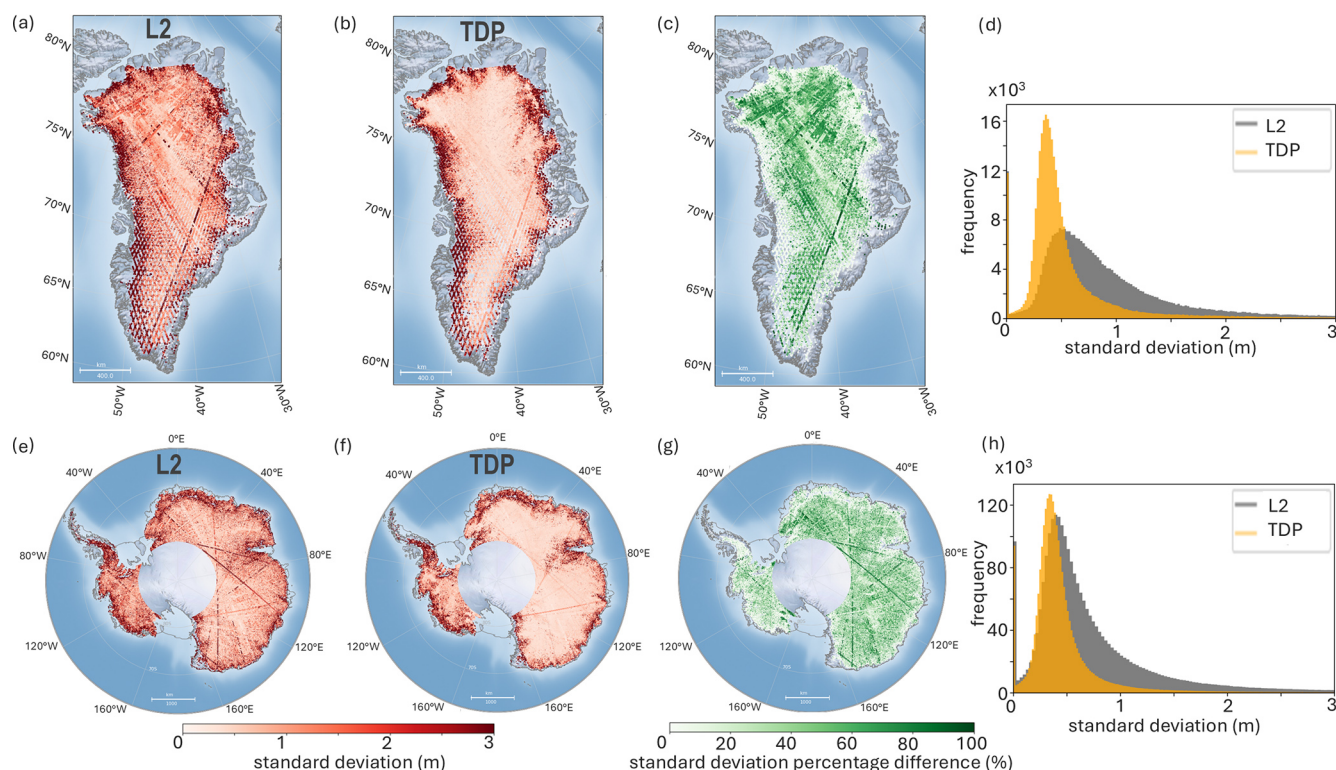
Figure 16. Assessment of the internal stability of the ERS-1 FDR4ALT Level-2 and TDP products for acquisitions over the Greenland **(a–d)** and Antarctic **(e–h)** ice sheets. The panels show: the temporal standard deviation for the Level-2 product (**a** and **e**); the temporal standard deviation for the TDP product (**b** and **f**); the percentage improvement in standard deviation between the Level-2 and TDP products (**c** and **g**); and the distribution of standard deviation for all tracks for Greenland (**d**) and Antarctica (**h**), and for the Level-2 product (grey) and the TDP product (orange).

ing modest improvements in terms of reducing both the magnitude of the elevation bias (10 cm improvement) and the MAD (5 cm improvement).

3.2.3 ERS-1

Finally, we performed the same analysis for the ERS-1 processing configurations. Figure 10 shows maps of ERS-1 elevation differences with respect to the reference data and Fig. 11 presents density scatter plots of their respective distributions. Comparing the statistics (Table 7), we find that although the FDR4ALT solutions exhibit a larger bias than the REAPER product, they deliver both a modest reduction in the MAD dispersion (a 6 % reduction for the TCOG solution) and the proportion of outliers (from 14 % to 11 %). The density scatter plots shown in Fig. 11 demonstrate similar behaviour to Envisat and ERS-2, with REAPER exhibiting an increasingly positive bias at lower elevations. As was the case for both Envisat and ERS-2, the FDR4ALT solutions successfully removes this artefact. Finally, comparing the two FDR4ALT configurations shows that the TCOG solution offers a slightly lower dispersion (0.76 cm vs 0.81 cm, for TCOG and TFMRA, respectively), whereas the

TFMRA solution delivers a lower magnitude bias (−0.81 cm vs −0.36 cm, for TCOG and TFMRA, respectively).

3.2.4 Influence of surface slope

In the previous analysis, we determined performance metrics that were aggregated at the ice sheet scale. Next, in order to better understand the impact of surface topography, we assessed measurement accuracy as a function of ice sheet surface slope. We performed the assessment for each satellite mission, in each case comparing the performance of the new FDR4ALT datasets (TCOG solution) with the preceding baseline products (Fig. 12). Whilst the performance is broadly similar across the very lowest slopes of the interior of the ice sheet, it can be seen that the new FDR4ALT solution is much more robust in the increasingly steeper sloped regions of the ice margin. For slopes greater than ∼ 0.25°, the FDR4ALT solution delivers increasingly significant reductions in both the median absolute bias and the dispersion of the elevation differences relative to the airborne datasets. This is likely due to the implementation of a more sophisticated echo relocation methodology (Roemer et al., 2007) within the FDR4ALT processor, which provides a more realistic estimate of the true echoing point in areas
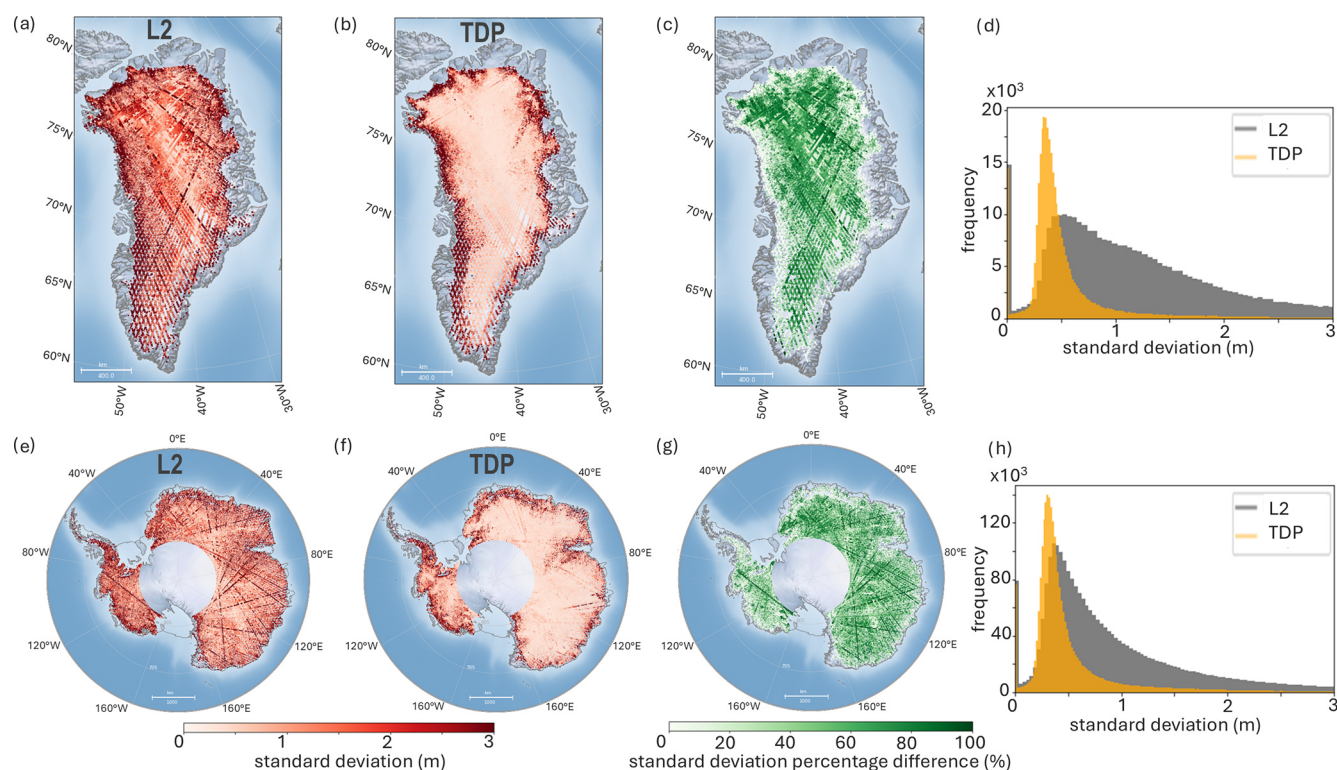
Figure 17. Assessment of the internal stability of the ERS-2 FDR4ALT Level-2 and TDP products for acquisitions over the Greenland **(a–d)** and Antarctic **(e–h)** ice sheets. The panels show: the temporal standard deviation for the Level-2 product (**a** and **e**); the temporal standard deviation for the TDP product (**b** and **f**); the percentage improvement in standard deviation between the Level-2 and TDP products (**c** and **g**); and the distribution of standard deviation for all tracks for Greenland (**d**) and Antarctica (**h**), and for the Level-2 product (grey) and the TDP product (orange).

of rugged topography, in combination with the FDR4ALT filtering and quality control. Comparing the performance of the FDR4ALT products across the three missions shows an apparent lower accuracy of Envisat at higher slopes, which is likely to reflect the increased coverage that Envisat achieves in these regions (Table 7).

3.3 Assessment of waveform morphology and impact upon measurement accuracy

It is well established that variable surface topography and backscattering characteristics within the altimeter beam footprint impact the shape of the returned waveform and cause divergence away from the classical Brownian-shaped echo. We therefore used our neural network classification of waveform type to investigate (1) how ERS-1, ERS-2, and Envisat waveform morphology varied over the Greenland and Antarctic ice sheets and (2) the impact of waveform shape upon measurement accuracy.

3.3.1 Audit of waveform class

As described previously, our neural network classifier was used to distinguish a number of common classes of wave-

form type. The proportion of waveforms within each class is summarised in Tables 8 and 9 and the spatial distributions of waveform types are shown in Figs. 13 and 14 for Greenland and Antarctica, respectively. Across Greenland and Antarctica, ERS-1 and ERS-2 exhibit similar spatial distributions, which is unsurprising given the similarity of their instruments and modes of acquisition. Across the interiors of both ice sheets, ERS waveforms largely fall within classes 1, 6, and 13, corresponding to a Brownian-type echo, with or without an additional peak close to the leading edge. The most notable divergence from this broad characterisation occurs within the interior of East Antarctica, where ERS-2 shows a greater proportion of Brownian echoes without an additional peak in comparison to ERS-1. Closer to the ice margin, the most dominant class for both ERS-1 and ERS-2 is class 13, indicating a Brownian-type shape with either a noisy leading edge or an indistinct trailing edge. In contrast, Envisat exhibits greater variance in the observed waveform shapes, potentially due to the prevalence of higher bandwidth acquisitions compared to ERS-1 and ERS-2 (Fig. 1) which allows more variability in the backscattered power to be resolved. Specifically, classes 1 and 7 are most common within the interior of both ice sheets, corresponding to classical
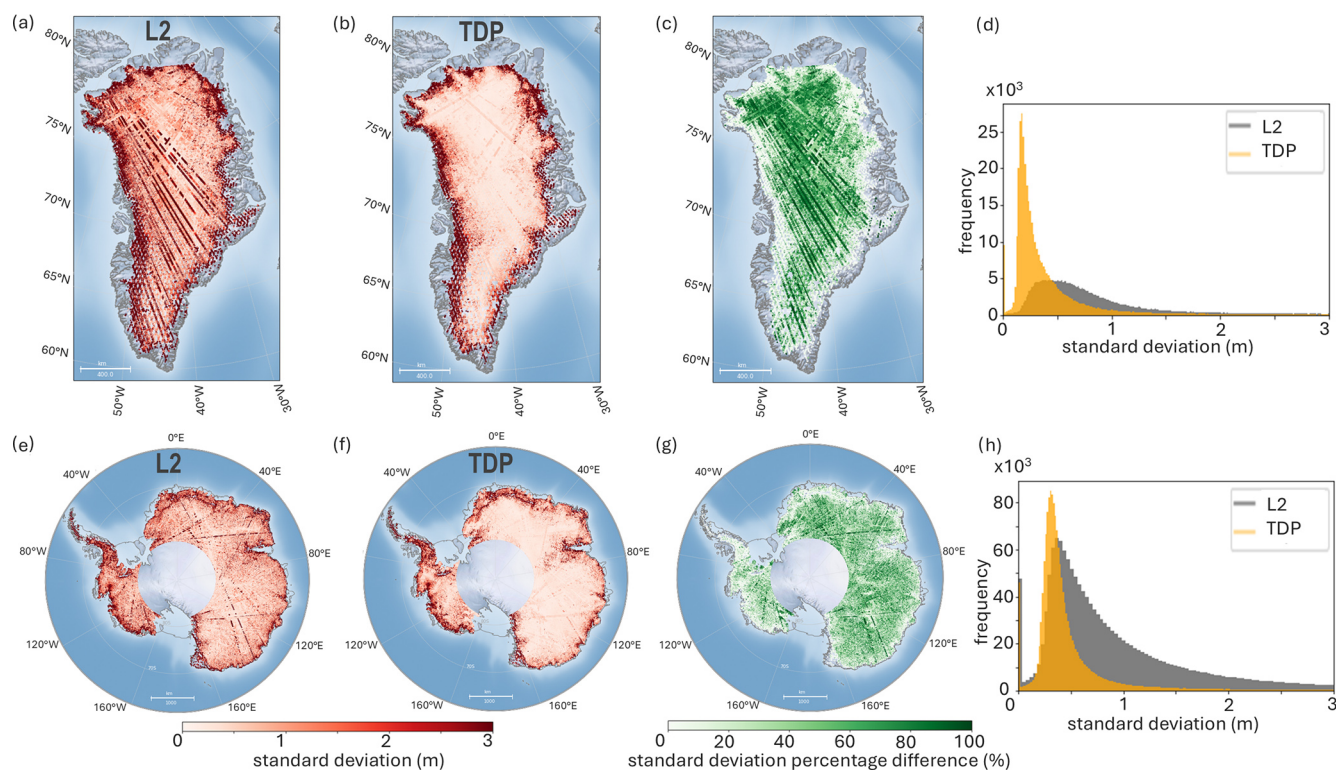
Figure 18. Assessment of the internal stability of the Envisat FDR4ALT Level-2 and TDP products for acquisitions over the Greenland **(a–d)** and Antarctic **(e–h)** ice sheets. The panels show: the temporal standard deviation for the Level-2 product (**a** and **e**); the temporal standard deviation for the TDP product (**b** and **f**); the percentage improvement in standard deviation between the Level-2 and TDP products (**c** and **g**); and the distribution of standard deviation for all tracks for Greenland (**d**) and Antarctica (**h**), and for the Level-2 product (grey) and the TDP product (orange).

Brownian-type echoes, and echoes with a less rapidly attenuating trailing edge. Moving towards the ice margins, Envisat waveform classes 9 and 11 become most dominant across both Greenland and Antarctica, corresponding to waveforms that have a very complex structure or a double or stepped leading edge.

3.3.2 Impact of waveform class on measurement accuracy

Next, for each mission we evaluated the impact of waveform morphology upon the derived elevation accuracy by partitioning the statistics from our accuracy assessment (Sect. 3.2) according to waveform class. This analysis allowed us to identify classes of waveforms that typically offer degraded performance using current processing approaches and therefore determine where there may be scope to make algorithmic improvements in the future. Across all missions, waveform classes 1, 5, 6, and 7 show relatively high levels of accuracy (Fig. 15), with median values close to zero and relatively low levels of dispersion. These waveform classes correspond to broadly Brownian-type echoes, with some distortion to the classical shape due to a more prominent peak or more slowly decaying trailing edge. These phenomena arise

due to the more complex nature of ice surfaces relative to ocean surfaces, with more variable footprint scale topography and greater penetration of the radar wave into the near surface snowpack. Nonetheless, the relatively good performance demonstrates the robustness of the empirical retracking and relocation approaches that have been implemented here. In contrast, multipeaked (class 3) waveforms generally produce a negative elevation bias, although the degradation in performance is less severe for Envisat than the preceding missions. For ERS-1 and ERS-2, the most common remaining classes are 9 (very complex) and 13 (disturbed leading edge). Whilst the accuracy of elevation measurements derived from class 13 waveforms is reasonable, class 9 waveforms exhibit a significant negative bias and large spread relative to coincident airborne data. For Envisat, in addition to classes 1, 3, and 7, the other most common classes are 9 (very complex; 2nd most common class) and 11 (stepped leading edge; 3rd most common class). In both cases, the accuracy of the associated elevation measurements remains relatively good, albeit with a small number of large outliers where the waveform complexity has not been adequately handled by the Level 2 processing. Overall, this analysis suggests that there may be scope to develop more sophisticated Level 2

Table 7. Performance metrics summarising the differences in elevation between ERS-1, ERS-2, and Envisat and contemporaneous airborne reference data. For each mission, statistics are provided for the baseline REAPER and Envisat version 3 products, together with the FDR4ALT TCOG and TFMRA retracking configurations. *Percentage of outliers* is defined as the percentage of measurements that deviate by more than 10 m from the corresponding airborne measurement of elevation.

Envisat	Version 3	FDR4ALT TCOG	FDR4ALT TFMRA
Percentage of valid elevation measurements	96.1 %	93.6 %	93.7 %
Number of comparison points	8560	7534	7548
Median elevation difference (m)	2.25	−0.51	−0.49
Median absolute deviation of the elevation differences (m)	2.41	0.80	0.78
Percentage of outliers	34.5 %	13.0 %	14.3 %
ERS-2	REAPER	FDR4ALT TCOG	FDR4ALT TFMRA
Percentage of valid elevation measurements	91.6 %	90.0 %	92.0 %
Number of comparison points	4778	4503	4504
Median elevation difference (m)	0.93	−0.25	−0.35
Median absolute deviation of the elevation differences (m)	0.87	0.84	0.89
Percentage of outliers	16.8 %	9.3 %	9.7 %
ERS-1	REAPER	FDR4ALT TCOG	FDR4ALT TFMRA
Percentage of valid elevation measurements	92.7 %	91.1 %	92.9 %
Number of comparison points	12 754	12 255	12 308
Median elevation difference (m)	0.17	−0.81	−0.36
Median absolute deviation of the elevation differences (m)	0.82	0.76	0.81
Percentage of outliers	13.8 %	10.7 %	10.7 %

processing approaches – targeting the retracking and relocation steps – that are specifically designed to handle complex, multi-peaked waveforms; this could yield further improvements in measurement accuracy over complex topographic regions in the future.

3.4 Thematic data product assessment

As described previously, one of the principal objectives of the TDP is to produce a more consistent product through time by correcting for topographically-induced elevation differences resulting from the orbital drift of the satellite. As such, we evaluate the TDP elevation measurements by assessing their stability through time. Ultimately, this attribute is beneficial for the reliable determination of ice sheet evolution and therefore this assessment allows us to determine the extent to which the TDP processing chain has improved upon the existing Level-2 product in terms of delivering a more consistent dataset, particularly for the non-altimetry expert user. More specifically, our assessment of the TDP was performed

by computing the temporal standard deviation of elevations across orbit cycles, at defined intervals along satellite tracks. The assessment was performed for all tracks crossing Greenland and Antarctica and for each of the three missions. In the case of ERS-1, we computed the standard deviation for only data acquired whilst in its 35 d orbit, to ensure that it most closely matched the orbital configuration of ERS-2 and Envisat, and thus provided consistency across the three satellite missions. In all cases the metrics were computed for both the FDR4ALT Level-2 and TDP products to assess the impact of the additional TDP processing. This analysis shows that the TDP achieves a much lower temporal standard deviation in elevation, in comparison to the Level-2 product, for both Greenland and Antarctica and across all missions (Figs. 16, 17, and 18 for ERS-1, ERS-2, and Envisat, respectively).

3.5 Limitations and opportunities for future research

In this study we have performed significant evolutions to the Level-2 and Level-2+ processing of historical radar altime-

Table 8. The percentage of waveforms within each class across the Greenland Ice Sheet, for ERS-1, ERS-2, and Envisat data. The number in brackets indicates the 5 most common waveform classes, with 1 indicating the most prevalent class.

Waveform class number	Description	ERS-1 (%)	ERS-2 (%)	Envisat (%)
1	Brownian	10.29 (3)	13.28 (3)	13.61 (4)
2	Highly specular	0.46	0.29	0.26
3	Multiple peaks	4.22 (5)	2.78	7.52 (5)
4	Moderately specular	0.63	0.34	0.06
5	Brownian with a peak on the trailing edge	8.02(4)	7.95 (4)	1.2
6	Brownian with a peak on the leading edge or a steep trailing edge	49.40 (1)	44.41 (1)	2.68
7	Brownian with a flat trailing edge	0.55	0.87	26.44 (2)
8	Strong peak at the end of the analysis window	–	–	0.23
9	Very complex echo	4.09	5.13 (5)	26.55 (1)
10	Brownian with high thermal noise	1.07	1.26	–
11	Double leading edge	3.37	3.08	16.44 (3)
12	Shifted Brownian	–	–	0.07
13	Brownian with a disturbed leading edge	13.26 (2)	15.03 (2)	–
14	Volume-Brownian	–	–	–
15	Linear rise	2.5	3.83	–
16	Right-shifted Brownian waveform	0.44	0.36	0.14
17	Breakage on the leading edge of a Brownian waveform	0.46	0.38	–
18	Linear decrease	1.16	0.93	–
19	Small step before leading edge	–	–	–
20	Peaky echo before a Brownian waveform	–	–	–

try data over ice sheets and, through extensive evaluation, shown the associated benefits in terms of the resultant product quality. Looking towards future work, the results of our validation have also highlighted potential opportunities for further improvements and avenues for additional research that may help to overcome remaining limitations. Compared to airborne data, we find that all missions exhibit an overall negative bias ranging from −0.25 to −0.81 m (Table 7). This negative bias is consistent with our understanding that Ku-band energy penetrates into the near-surface snowpack, and is thus more explainable than the positive elevation biases ranging from 0.17 to 2.25 metres that were observed in the REAPER and Envisat version 3 datasets. Nonetheless, building on our analysis presented here, it would be beneficial for future work to target (1) a better understanding of the source of the remaining variation in biases between the different missions and (2) additional algorithm development to further reduce the magnitudes of these biases, such that the retrieved elevation is closer to the air-snow interface. In the case of the latter point, this could involve further assessment and tuning of the empirical retrackers and relocation methods deployed within this study or undertaking more fundamental development and optimisation of physically-based ice sheet retracking strategies.

In terms of measurement precision, it is encouraging that with our consistent processing approach we now obtain similar levels of (1) MAD dispersion and (2) proportion of outliers across all missions, with these statistics being within 8 cm and 4 % of each other, respectively, for all three missions (Table 7). This represents a significant improvement in inter-mission consistency compared to previous products. As a result, elevation measurements derived from all missions now exhibit a MAD dispersion relative to airborne data of ∼ 0.8 m, with ∼ 10 % of measurements classed as outliers;

Table 9. The percentage of waveforms within each class across the Antarctic Ice Sheet, for ERS-1, ERS-2, and Envisat data. The number in brackets indicates the top 5 waveform classes by percentage, with 1 indicating the most prevalent class.

Waveform class number	Description	ERS-1 (%)	ERS-2 (%)	Envisat (%)
1	Brownian	20.73 (2)	28.26 (2)	7.69 (4)
2	Highly specular	0.25	0.17	0.09
3	Multiple peaks	1.37	1.14	4.42 (5)
4	Moderately specular	0.09	0.05	0.01
5	Brownian with a peak on the trailing edge	7.58 (4)	6.98 (4)	0.86
6	Brownian with a peak on the leading edge or with a steep trailing edge	47.26 (1)	39.1 (1)	2.03
7	Brownian with a flat trailing edge	0.72	1.14	39.56 (1)
8	Strong peak at the end of the analysis window	–	–	0.13
9	Very complex echo	2.59 (5)	2.85 (5)	22.80 (2)
10	Brownian with high thermal noise	1.15	1.24	–
11	Stepped leading edge	2.19	1.92	14.55 (3)
12	Shifted Brownian	–	–	0.05
13	Brownian with a disturbed leading edge	12.64 (3)	13.41 (3)	–
14	Volume-Brownian	–	–	–
15	Linear rise	2.05	2.49	–
16	Right-shifted Brownian waveform	0.27	0.26	0.08
17	Breakage on the leading edge of a Brownian waveform	0.39	0.36	–
18	Linear decrease	0.64	0.35	–
19	Small step before leading edge	–	–	–
20	Peaky echo before a Brownian waveform	–	–	–

this is encouraging given that none of these missions were designed with ice sheet monitoring as a primary mission requirement. Looking towards avenues of future research, it will be beneficial for work to target further reductions in both of these statistics, which may be possible through additional innovations to the Level-2 processing algorithms. Based upon our analysis of waveform class, it is likely that efforts targeting robust processing of complex, multi-peaked waveforms may yield particular benefits. This may include developing and implementing new dedicated multi-peak retracking approaches (Huang et al., 2024), additional refinements to the existing Roemer relocation approach (Roemer et al., 2007), or deploying alternative relocation strategies such as waveform leading edge (Li et al., 2022) or facet-based numerical modelling (Aublanc et al., 2025) approaches. In all cases, it is clear that there is significant benefit in taking new methods that have been developed and deployed within

the context of current missions, such as CryoSat-2 (Li et al., 2022) and Sentinel-3 (Huang et al., 2024; Aublanc et al., 2025), and investigating their capacity to enhance the historical altimeter record. Finally, our hope is that the inclusion of an uncertainty parameter within the product will offer significant benefit to a wide range of end users. If indeed this is the case, then the implementation provided here should be viewed as a first step towards more sophisticated approaches of uncertainty estimation. Specifically, within this study, we have developed an empirical parameterisation of uncertainty based upon ice sheet surface slope. Going forward, it would be beneficial to further refine this approach by assessing and including more covariates within the parameterisation, such as surface roughness and waveform morphology, with the ultimate goal being to move towards formal bottom-up propagation of uncertainties from the Level-0 or Level-1b data themselves.

4 Conclusions

In this study, we have presented a new reprocessing of the ERS-1, ERS-2, and Envisat radar altimetry datasets over the ice sheets of Greenland and Antarctica. The reprocessing ingests Level-1b data, applies updated Level-2 processing that is tailored to ice sheets, and adds additional Level-2+ algorithms that generate for the first time a thematic data product, which is designed to be more accessible for the non-expert user. We perform a comprehensive assessment of the accuracy of these new datasets by comparing them to contemporaneous airborne measurements and evaluate changes in performance relative to the existing REAPER and Envisat version 3 baseline products. Overall, we find that the updated processing leads to a closer agreement with airborne data both in terms of the median bias and the dispersion of the differences. As part of the analysis, we compare results from two empirical retrackers and find only small differences in performance between the two. As such, we conclude that updates in other Level-2 processing steps, such as the algorithms used for echo relocation and quality control, exert a larger influence on overall measurement accuracy. We implement a neural network classifier to explore the different classes of waveform shape present over ice sheets and use this to show how measurement accuracy is affected by waveform morphology. The datasets generated in this study are publicly available from the Europe Space Agency and provide the opportunity for improved long-term constraint of ice sheet elevation change, mass imbalance, and, ultimately, a better understanding of the cryospheric contribution to sea level rise.

Author contributions. MM conceived and supervised the study. MRS, JM, FP, JA, QH, JAD, and CG processed the data and performed the experiments. JAD developed and validated the AI algorithm. MRS, MM, JM, FP, JA, and JAD drafted the manuscript. All authors contributed to the analysis of the results and commented on the manuscript.

Competing interests. The contact author has declared that none of the authors has any competing interests.

Disclaimer. Publisher's note: Copernicus Publications remains neutral with regard to jurisdictional claims made in the text, published maps, institutional affiliations, or any other geographical representation in this paper. While Copernicus Publications makes every effort to include appropriate place names, the final responsibility lies with the authors.

Review statement. This paper was edited by Benjamin Smith and reviewed by two anonymous referees.

References

Aublanc, J., Boy, F., Borde, F., and Féménias, P.: A facet-based numerical model to retrieve ice sheet topography from Sentinel-3 altimetry, The Cryosphere, 19, 1937–1954, https://doi.org/10.5194/tc-19-1937-2025, 2025.

Bamber, J. L.: Ice sheet altimeter processing scheme, Int. J. Remote Sens., 15, 925–938, https://doi.org/10.1080/01431169408954125, 1994.

Bamber, J. L., Gomez-Dans, J. L., and Griggs, J. A.: A new 1 km digital elevation model of the Antarctic derived from combined satellite radar and laser data – Part 1: Data and methods, The Cryosphere, 3, 101–111, https://doi.org/10.5194/tc-3-101-2009, 2009.

Bamber, J. L., Griggs, J. A., Hurkmans, R. T. W. L., Dowdeswell, J. A., Gogineni, S. P., Howat, I., Mouginot, J., Paden, J., Palmer, S., Rignot, E., and Steinhage, D.: A new bed elevation dataset for Greenland, The Cryosphere, 7, 499–510, https://doi.org/10.5194/tc-7-499-2013, 2013.

Brockley, D. J., Baker, S., Femenias, P., Martinez, B., Massmann, F., Otten, M., Paul F., Picard B., Prandi P., Roca M., Rudenko S., Scharroo R. and Visser, P.: REAPER: Reprocessing 12 years of ERS-1 and ERS-2 altimeters and microwave radiometer data, IEEE T. Geosci. Remote, 55, 5506–5514, https://doi.org/10.1109/tgrs.2017.2709343, 2017.

Casella, D.: Product Quality README file for ENVISAT RA-2/MWR Level 2 V3.0 dataset (ESA-EOPG-MOM-TN-15), https://earth.esa.int/eogateway/documents/20142/37627/Envisat-RA-2-MWR-Level-2-Product-Readme-3.pdf, last access: 30 June 2018.

Dawson, G. J. and Bamber, J. L.: Antarctic Grounding Line mapping from CryoSat-2 Radar Altimetry, Geophys. Res. Lett., 44, 11886–11893, https://doi.org/10.1002/2017gl075589, 2017.

de Q. Robin, G.: Mapping the Antarctic ice sheet by satellite altimetry, Can. J. Earth Sci., 3, 893–901, https://doi.org/10.1139/e66-072, 1966.

European Space Agency (ESA): FDR4ALT Land-Ice Thematic Data Product, Version 1.0, ESA [data set], https://earth.esa.int/eogateway/catalog/tdp-for-land-ice (last access: 22 July 2025), 2023.

FDR4ALT team: FDR4ALT Detailed Processing Model Document, https://earth.esa.int/documents/d/earth-online/fdr4alt-detailed-processing-model, 5 June 2023.

Helm, V., Humbert, A., and Miller, H.: Elevation and elevation change of Greenland and Antarctica derived from CryoSat-2, The Cryosphere, 8, 1539–1559, https://doi.org/10.5194/tc-8-1539-2014, 2014.

Hogg, A. E., Shepherd, A., Gilbert, L., Muir, A., and Drinkwater, M. R.: Mapping ice sheet grounding lines with CryoSat-2, Adv. Space Res., 62, 1191–1202, https://doi.org/10.1016/j.asr.2017.03.008, 2018.

Howat, I. M., Porter, C., Smith, B. E., Noh, M.-J., and Morin, P.: The Reference Elevation Model of Antarctica, The Cryosphere, 13, 665–674, https://doi.org/10.5194/tc-13-665-2019, 2019.

Huang, Q., McMillan, M., Muir, A., Phillips, J., and Slater, T.: Multipeak retracking of radar altimetry waveforms over ice sheets, Remote Sens. Environ., 303, 114020, https://doi.org/10.1016/j.rse.2024.114020, 2024.

The IMBIE Team: Mass balance of the Antarctic Ice Sheet from 1992 to 2017, Nature, 558, 219–222, https://doi.org/10.1038/s41586-018-0179-y, 2018

The IMBIE Team: Mass balance of the Greenland Ice Sheet from 1992 to 2018, Nature, 579, 233–239, https://doi.org/10.1038/s41586-019-1855-2, 2019.

Konrad, H., Shepherd, A., Gilbert, L., Hogg, A. E., McMillan, M., Muir, A., and Slater, T.: Net retreat of Antarctic glacier grounding lines, Nat. Geosci., 11, 258–262, https://doi.org/10.1038/s41561-018-0082-z, 2018.

Krabill, W. B., Thomas, R. H., Martin, C. F., Swift, R. N., and Frederick, E. B.: Accuracy of airborne laser altimetry over the Greenland ice sheet, Int. J. Remote Sens., 16, 1211–1222, https://doi.org/10.1080/01431169508954472, 1995.

Li, W., Slobbe, C., and Lhermitte, S.: A leading-edge-based method for correction of slope-induced errors in ice-sheet heights derived from radar altimetry, The Cryosphere, 16, 2225–2243, https://doi.org/10.5194/tc-16-2225-2022, 2022.

Martin, C. F., Krabill, W. B., Manizade, S. S., Russell, R. L., Sonntag, J. G., Swift, R. N., and Yungel, J. K.: Airborne Topographic Mapper Calibration Procedures and Accuracy Assessment, Goddard Space Flight Center, https://ntrs.nasa.gov/api/citations/20120008479/downloads/20120008479.pdf (last access: 23 July 2025), 2012.

McMillan, M., Corr, H., Shepherd, A., Ridout, A., Laxon, S., and Cullen, R.: Three-dimensional mapping by CryoSat-2 of subglacial lake volume changes, Geophys. Res. Lett., 40, 4321–4327, https://doi.org/10.1002/grl.50689, 2013.

McMillan, M., Shepherd, A., Sundal, A., Briggs, K., Muir, A., Ridout, A., Hogg, A., and Wingham, D.: Increased ice losses from Antarctica detected by CryoSat-2, Geophys. Res. Lett., 41, 3899–3905, https://doi.org/10.1002/2014gl060111, 2014.

McMillan, M., Leeson, A., Shepherd, A., Briggs, K., Armitage, T. W. K., Hogg, A., Kuipers Munneke, P., van den Broeke, M., Noël, B., van de Berg, W. J., Ligtenberg, S., Horwath, M., Groh, A., Muir, A., and Gilbert, L.: A high-resolution record of Greenland mass balance. Geophys. Res. Lett., 43, 7002–7010, https://doi.org/10.1002/2016gl069666, 2016.

McMillan, M., Muir, A., Shepherd, A., Escolà, R., Roca, M., Aublanc, J., Thibaut, P., Restano, M., Ambrozio, A., and Benveniste, J.: Sentinel-3 Delay-Doppler altimetry over Antarctica, The Cryosphere, 13, 709–722, https://doi.org/10.5194/tc-13-709-2019, 2019.

McMillan, M., Muir, A., and Donlon, C.: Brief communication: Ice sheet elevation measurements from the Sentinel-3A and Sentinel-3B tandem phase, The Cryosphere, 15, 3129–3134, https://doi.org/10.5194/tc-15-3129-2021, 2021.

Milligan, D., Gratadour, J., Emanuelli, P. P., Diekmann, F., Mesples, D., Lerch, J., Bozzi, V., and Lengert, W.: ERS-2 Ground Segment and Operations evolution, in: Space Ops 2008 Conference, Heidelberg, Germany, 12–16 May 2008, https://doi.org/10.2514/6.2008-3472, 2008.

Moholdt, G., Nuth, C., Hagen, J. O., and Kohler, J.: Recent elevation changes of Svalbard glaciers derived from ICESat laser altimetry, Remote Sen. Environ., 114, 2756–2767, https://doi.org/10.1016/j.rse.2010.06.008, 2010.

Morlighem, M., Rignot, E., Binder, T., Blankenship, D., Drews, R., Eagles, G., Eisen, O., Ferraccioli, F., Forsberg, R., Fretwell, P., Goel, V., Greenbaum, J. S., Gudmundsson, H., Guo, J., Helm, V., Hofstede, C., Howat, I., Humbert, A., Jokat, W., Karlsson, N. B., Lee, W. S., Matsuoka, K., Millan, R., Mouginot, J., Paden, J., Pattyn, F., Roberts, J., Rosier, S., Ruppel, A., Seroussi, H., Smith, E. C., Steinhage, D., Sun, B., van den Broeke, M. R., van Ommen, T. D., van Wessem, M., and Young, D. A.: Deep glacial troughs and stabilizing ridges unveiled beneath the margins of the Antarctic ice sheet, Nat. Geosci., 13, 132–137, https://doi.org/10.1038/s41561-019-0510-8, 2020.

Otosaka, I., Shepherd, A., and McMillan, M.: Ice sheet elevation change in West Antarctica from Ka-Band satellite Radar Altimetry, Geophys. Res. Lett., 46, 13135–13143, https://doi.org/10.1029/2019gl084271, 2019.

Otten, X. and Visser, P.: ERS orbit validation report, https://earth.esa.int/eogateway/documents/20142/37627/ERS-Orbit-Validation-Report.pdf (last access: 23 July 2025), 2019.

Peacock, N. R.: Arctic sea ice and ocean topography from satellite altimetry, PhD Thesis, University College London, https://discovery.ucl.ac.uk/id/eprint/10100088 (last access: 23 July 2025), 1998.

Picot, N., Marechal C., Couhert A., Desai S., Scharroo R., and Egido A.: Jason-3 Products Handbook, SALP-MU-M-OP-16118-CN, https://www.ospo.noaa.gov/Products/documents/hdbk_j3.pdf, last access: September 2018.

Piras, F., Daguzé J. A., Fréry M. L., Roinard H., Ollivier A., Quet V., Calmettes B., McMillan M., Picard B., Fell F., Bennartz R., Fleury S., Nino F., Salila H., Tarpanelli A.: FDR4ALT Product User Guide, CLS-ENV-MU-23-0237, https://earth.esa.int/eogateway/documents/d/earth-online/fdr4alt-products-user-guide, last access: October 2023.

Poisson, J., Quartly, G. D., Kurekin, A. A., Thibaut, P., Hoang, D., and Nencioli, F.: Development of an ENVISAT Altimetry processor providing sea level continuity between open ocean

and Arctic leads, IEEE T. Geosci. Remote, 56, 5299–5319, https://doi.org/10.1109/tgrs.2018.2813061, 2018.

Porter, C., Morin, P., Howat, I., Noh, M. J., Bates, B., Peterman, K., Keesey, S., Schlenk, M., Gardiner, J., Tomko, K., Willis, M., Kelleher, C., Cloutier, M., Husby, E., Foga, S., Nakamura, H., Platson, M., Wethington, M. Jr., Williamson, C., Bauer, G., Enos, J., Arnold, G., Kramer, W., Becker, P., Doshi, A., D'Souza, C., Cummens, P., Laurier, F., and Bojesen, M.: ArcticDEM, Version 3, Harvard Dataverse [data set] https://doi.org/10.7910/dvn/ohhukh, 2018.

Pörtner, H.-O., Roberts, D., Masson-Delmotte, V., Zhai, P., Tignor, M., Poloczanska, E., Mintenbeck, K., Alegría, A., Nicolai, M., Okem, A., Petzold, J., Rama, B., and Weyer, N. (Eds.): IPCC Special Report on the Ocean and Cryosphere in a Changing Climate, Cambridge University Press, Cambridge, UK and New York, NY, USA, https://doi.org/10.1017/9781009157964, 2019.

Roca, M., Laxon, S., and Zelli, C.: The EnViSAT RA-2 instrument design and tracking performance, IEEE T. Geosci. Remote, 47, 3489–3506, https://doi.org/10.1109/tgrs.2009.2020793, 2009.

Roemer, S., Legresy, B., Horwath, M., and Dietrich, R.: Refined analysis of radar altimetry data applied to the region of the subglacial Lake Vostok/Antarctica, Remote Sens. Environ., 106, 269–284, https://doi.org/10.1016/j.rse.2006.02.026, 2007.

Schröder, L., Horwath, M., Dietrich, R., Helm, V., van den Broeke, M. R., and Ligtenberg, S. R. M.: Four decades of Antarctic surface elevation changes from multi-mission satellite altimetry, The Cryosphere, 13, 427–449, https://doi.org/10.5194/tc-13-427-2019, 2019.

Shepherd, A., Gilbert, L., Muir, A. S., Konrad, H., McMillan, M., Slater, T., Briggs, K. H., Sundal, A. V., Hogg, A. E., and Engdahl, M. E.: Trends in Antarctic ice sheet elevation and mass, Geophy. Res. Lett., 46, 8174–8183, https://doi.org/10.1029/2019gl082182, 2019.

Simeon, M., Frery M. L., Daguze J. A., and Piras F.: FDR4ALT validation report document, CLS-ENV-NT-23-0426, https://earth.esa.int/documents/d/earth-online/fdr4alt-validation-report-fdr (last access: 4 July 2023), 2023.

Simonsen, S. B., Barletta, V. R., Colgan, W. T., and Sørensen, L. S.: Greenland Ice Sheet Mass Balance (1992–2020) from calibrated Radar Altimetry, Geophys. Res. Lett., 48, e2020GL091216, https://doi.org/10.1029/2020gl091216, 2021.

Slater, T., Shepherd, A., McMillan, M., Muir, A., Gilbert, L., Hogg, A. E., Konrad, H., and Parrinello, T.: A new digital elevation model of Antarctica derived from CryoSat-2 altimetry, The Cryosphere, 12, 1551–1562, https://doi.org/10.5194/tc-12-1551-2018, 2018.

Slater, T., Shepherd, A., McMillan, M., Leeson, A., Gilbert, L., Muir, A., Kuipers Munneke, P., Noël, B., Fettweis, X., van den Broeke, M., and Briggs, K.: Increased variability in Greenland Ice Sheet runoff from satellite observations, Nat. Commun., 12, 6069, https://doi.org/10.1038/s41467-021-26229-4, 2021.

Sørensen, L. S., Simonsen, S. B., Nielsen, K., Lucas-Picher, P., Spada, G., Adalgeirsdottir, G., Forsberg, R., and Hvidberg, C. S.: Mass balance of the Greenland ice sheet (2003–2008) from ICESat data – the impact of interpolation, sampling and firn density, The Cryosphere, 5, 173–186, https://doi.org/10.5194/tc-5-173-2011, 2011.

Sørensen, L. S., Simonsen, S. B., Forsberg, R., Khvorostovsky, K., Meister, R., and Engdahl, M. E.: 25 years of elevation changes of the Greenland Ice Sheet from ERS, Envisat, and CryoSat-2 radar altimetry, Earth Planet. Sc. Lett., 495, 234–241, https://doi.org/10.1016/j.epsl.2018.05.015, 2018.

Soussi, B., Urien S., Picard B., Muir A., Roca M., and Garcia P.: Envisat Altimetry Level 2 Product Handbook, CLS-ESLF-18-0003, https://earth.esa.int/eogateway/documents/20142/37627/Envisat-RA-2-Level-2-Product-Handbook.pdf, last access: March 2018.

Venables, W. N. and Ripley, B. D.: Modern Applied Statistics with S, Springer New York, NY, https://doi.org/10.1007/978-0-387-21706-2, 2002.

Wingham, D. J., Rapley, C. G., and Griffiths, H.: New techniques in satellite altimeter tracking systems, in: Proceedings of the IGARSS Symposium, Zurich, Switzerland, 8–11 September 1986, https://www.researchgate.net/profile/Chris-Rapley/publication/269518510_New_Techniques_in_Satellite_Altimeter_Tracking_Systems/links/55b5e51a08aec0e5f436c3f7/New-Techniques-in-Satellite-Altimeter-Tracking-Systems.pdf (last access: 22 July 2025), 1986.

Wingham, D. J., Ridout, A. J., Scharroo, R., Arthern, R. J., and Shum, C. K.: Antarctic Elevation Change from 1992 to 1996, Science, 282, 456–458, https://doi.org/10.1126/science.282.5388.456, 1998.

Wingham, D. J., Siegert, M. J., Shepherd, A., and Muir, A. S.: Rapid discharge connects Antarctic subglacial lakes, Nature, 440, 1033–1036, https://doi.org/10.1038/nature04660, 2006a.

Wingham, D. J., Shepherd, A., Muir, A., and Marshall, G. J.: Mass balance of the Antarctic ice sheet, Philos. T. R. Soc. A, 364, 1627–1635, https://doi.org/10.1098/rsta.2006.1792, 2006b.

Zwally, H. J., Li, J., Robbins, J. W., Saba, J. L., Yi, D., and Brenner, A. C.: Mass gains of the Antarctic ice sheet exceed losses, J. Glaciol., 61, 1019–1036, https://doi.org/10.3189/2015jog15j071, 2015.